Acoustic Manipulations of Micro-robots with Visual Servoing Feedback Control

POLITECNICO
MILANO 1863

present on 21 Dec 2021
Polytechnic University of Milan **POLIMI**
Acoustic Robotics Systems Lab
Swiss Federal Institute of Technology in Zürich **ETH**

Mahmoud Medany

Prof Ferruccio Resta, Rector
Prof Luca Bascetta, Thesis director
Prof Daniel Ahmed, Thesis director

ETH zürich

Milano, POLIMI, 2021

Abstract

Micro/nano-robots have the potential to create new opportunities in targeted and precise drug delivery. Acoustics with the ability to generate forces wirelessly will make existing therapeutic and diagnostic procedures less invasive and enable new methods never before possible. This thesis is written with the objective to research the possibilities of visual servoing control applied to acoustic applications. In particular, in this work, precise manipulation for micro-nano robots in microfluidic channels under the case of stagnant or chaotic flow has been considered. Furthermore, the visual feedback control system allowed the micro-robots to either autonomously or semi-autonomously perform a specific task in a complex environment. The project has been developed in partnership with Politecnico di Milano and ETH Zurich.

The first step focused on analyzing the physical model of the micro-robots, which are microbubbles based on the resonant acoustic field, and then the mathematical model of the acoustic radiation forces generated by this field. In particular, in view of the design specifications, the dynamics of the system have been identified. Subsequently, the mathematical equations describing the attraction forces between microrobots have been analyzed, which created the swarming of the microrobots.

After analyzing the model, several experimental setups have been used to test the control system in different environments and with various actuator positions. Subsequently, the control circuits have been described with the use of a custom-made driver for a function generator that generates the AC signals for the piezo transducers to transform them to an acoustic field. Afterward, the image acquisition and processing have been defined for object detection and tracking with assigning a specific ID for each micro-robot swarm while targeting to move the largest swarm to the destination.

The resulting features extracted were then used in the different operating modes of the controller. The image-based visual servoing controller has shown difficulty in reaching the final target following a predefined path due to the unexpected dynamics of the system. To deal with the difficulties of driving the micro-robots, a state machine controller has been designed to keep the speed of the micro-robot swarms constant all over the channel, Additionally driving the micro-robots to stick to the wall to reduce the drag force affecting them while moving towards the target.

Sommario

I micro/nano-robot hanno il potenziale per creare nuove opportunità nella somministrazione mirata e precisa dei farmaci. L'acustica, con la capacità di generare forze in modalità wireless, renderà le procedure terapeutiche e diagnostiche esistenti meno invasive e consentirà l'uso di nuovi metodi fino ad oggi non possibili. Questa tesi è stata scritta con l'obiettivo di ricercare le possibilità del controllo del servocomando visivo applicato alle applicazioni acustiche. In particolare, in questo lavoro è stata considerata una manipolazione precisa per micro-nano robot in canali microfluidici in caso di flusso stagnante o caotico. Inoltre, il sistema di controllo del feedback visivo ha consentito ai microrobot di eseguire in modo autonomo o semi-autonomo un compito specifico in un ambiente complesso. Il progetto è stato sviluppato in collaborazione con il Politecnico di Milano e l'ETH di Zurigo.

Inizialmente è stata effettuata l'analisi del modello fisico dei microrobot, che sono microbolle basate sul campo acustico risonante, in seguito è stata svolta l'analisi del modello matematico delle forze di radiazione acustica generate da questo campo. Alla luce delle specifiche progettuali sono state individuate le dinamiche del sistema. Successivamente sono state analizzate le equazioni matematiche che descrivono le forze di attrazione tra i microrobot, che hanno creato lo sciame dei microrobot.

Dopo aver analizzato il modello, sono state utilizzate diverse configurazioni sperimentali per testare il sistema di controllo in diversi ambienti e con varie posizioni dell'attuatore. Successivamente sono stati descritti i circuiti di controllo con l'utilizzo di un driver su misura per un generatore di funzioni che genera i segnali AC per i trasduttori piezoelettrici per trasferirli in un campo acustico. Successivamente sono state definite l'acquisizione e l'elaborazione delle immagini per il rilevamento e il tracciamento degli oggetti con l'assegnazione di un ID specifico a ciascun microrobot durante il targeting al fine di spostare lo sciame più grande sul bersaglio.

Le caratteristiche risultanti estratte sono state poi utilizzate nelle diverse modalità operative del controllore. Il controller di asservimento visivo basato sulle immagini ha mostrato difficoltà nel raggiungere l'obiettivo finale seguendo un percorso predefinito a causa delle dinamiche inaspettate del sistema. Per far fronte alle difficoltà di guidare il micro-robot, è stato progettato un controller macchina di stato per mantenere costante la velocità degli sciami di micro-robot su tutto il canale, costringendo inoltre i micro-robot ad attaccarsi al muro per ridurre la forza di trascinamento influenzandoli mentre si spostano verso il bersaglio.

Contents

List of Figures

List of Tables

1 Introduction

1.1 Context

Micro-robotics technology forms an integral part of modern-day microsystem technology and provides prospects for diverse biomedical applications from tissue engineering to clinical diagnostic. Because of the untethered external actuation ability, the microrobot can move inside a human body and access the majority of locations to achieve accurate diagnosis and therapeutics as a distinguished mechanism from the conventional medical surgical robot (Soltani et al., 2017). Moreover, the microrobot can perform safe and minimally invasive treatment, thereby ensuring a low risk of infection and internal injuries through vessels.

To realize the concept, one of the most challenging yet essential issues has been to develop a dependable propulsion technique for the microrobots; this requires a different method from propulsion techniques used in macroscale environments (Nelson et al., 2010). In microscale environments, the relative importance of the physical effects relies on the surrounding environment, although the basic physics are constant. For example, surface tension dominate body forces such as inertial force and gravity, and the effect of the surrounding fluid viscosity can become significant (Beebe et al., 2002). Thus, tremendous efforts have been devoted to develop various micro propulsion techniques of microrobots based on optics (Ashkin and Dziedzic, 1987), magnetism (De Vlaminck and Dekker, 2012), plasmonics (Juan et al., 2011), acoustics (Shi et al., 2009) (Ozcelik et al., 2018) and acoustics combined with magnetics (Ahmed et al., 2017) have been exploited for remote actuation of synthetic and biological agents with such low-power and reliable actuation.

Optical tweezers have been one of the most fundamental technologies that employ focused laser beams to trap agents across a wide range of sizes (100 nm–1 mm). However, besides the high-priced and complex optical hardware required in optical tweezers, the high-power operation of lasers may destroy living or otherwise sensitive biological specimens. On the other hand, plasmonic tweezers are a low-power variant of optical tweezers capable of much finer nanomanipulation. However, they require a nanostructured substrate to control light beams for high-resolution traps and also suffer from heat dissipation into the surrounding

environment.

Magnetic tweezers are ubiquitous in DNA manipulation though they provide low resolution for video inspection via microscopy (Neuman and Nagy, 2008). The requirement for a high magnetic field or gradient burdens the instrumentation of magnetic tweezers. Moreover, collision-free navigation enabled by the magnetic field has been demonstrated to transport chemically powered Janus micromotors in a complex environment (Li et al., 2017). Furthermore, magnetic fields have been applied to actuate and control micro/nano-robots for payload transportation and drug delivery (Wu et al., 2018). These trade-offs necessitate a low-power actuation tool that offers a broad range of target sizes for micromanipulation.

Acoustic manipulation has emerged as a low power, biocompatible, and versatile technique that overcomes the limitations of other manipulation methods mentioned earlier. Furthermore, acoustic manipulation techniques exist in a broad operating frequency range of $100Hz$–$100MHz$. Consequently, acoustic actuation techniques can manipulate agents across several orders of magnitude in size, from clusters of nanoparticles up to millimeter-sized biological worms (Ahmed, Ozcelik, et al., 2016). Furthermore, this frequency range complements the working range of ultrasound imaging devices, making acoustic manipulation techniques suitable for medical applications. Importantly, most of the acoustic manipulation techniques use sound intensities of less than $10Wcm^{-2}$ on the target agents, which makes them safe for sensitive label-free handling of biological agents such as embryos and cells (Mohanty et al., 2020).

Over the past decades, acoustic micro-robot manipulation systems have been extensively studied from working mechanism analyses to device design and fabrications. Microrobots with diverse shapes were proposed to implement different modes of movement, such as the microbowl motors powered by hybrid light/acoustic fields with tunable locomotion and collective behavior (Tang et al., 2019). Additionally, Wang et al. further explored the modification of acoustically propelled nanowires coupled with DNA strands to accomplish the task of intracellular surgery (Esteban-Fernández de Ávila et al., 2016). Zhang et al. described a digital acoustofluidic device that allowed users to transport, merge, mix, and split reagents in a programmable and contactless manner(Zhang et al., 2018). Drinkwater et al. presented holographic acoustic tweezers capable of manipulating multiple particles individually (Marzo and Drinkwater, 2019). Huang et al. successfully demonstrated dynamic and reconfigurable manipulation of particles and cells with wavenumber-spiral acoustic tweezers(Tian et al., 2019). Inspired by biological organisms, Ahmed et al. described nano swimmers composed of a rigid bimetallic head and a flagellum-like flexible tail that achieves large-amplitude propulsion through the oscillation of the tail in traveling acoustic waves (Ahmed, Baasch, Jang, et al., 2016). Most recently, other micro swarm robots mimicking natural microswimmers were proposed to perform rolling-type motion (Ahmed, Ozcelik, et al., 2016). Xu et al. also studied the collective behavior of catalytic nanomotors to realize reversible swarming separation under acoustic field (Xu et al., 2015).

Although many advanced capabilities and sophisticated control have been achieved, there is still an unmet challenge for current acoustically powered microrobots to conduct accurate identification of the micro-nanorobots and automatic control of their dynamic motion which is strongly desired to develop the next generation of intelligent micro/nanorobots.

1.2 Overview

Regarding previous motivations, the objective of this work is to develop an acoustic micro-robotics manipulation interface that contains closed-loop visual servoing feedback control to manipulate micro-nanorobots with accurate target identification and tolerance definition. Governed by the vision feedback control method, this system can transport a single swarm of microrobots to the aimed point defined by users. Critical factors that affect the transporting performance have been experimentally explored and discussed with different positioning settings for tolerant values. At last, the precise positioning for microrobots is performed with the proposed platform to testify its biocompatibility and reproducibility for biological materials.

Chapter (2) treats the mathematical description of the acoustic radiation forces and how the bubbles interact and cluster into swarms.

Chapter (3) explains the system components and the different experimental setups to test the micro-robots.

Chapter (4) considers the image processing implementation of the microbots inside the microfluidic channel with different programming languages.

Chapter (5) describes the operating modes of the controller and visual servoing feedback controller.

Chapter (6) concludes the document by summarizing the work done in this thesis, discussing the validity of the obtained results, and proposing future work of research to enhance our results.

2 Acoustics and Radiation forces

2.1 Acoustic Waves

Acoustic waves are mechanical and longitudinal waves that result from an oscillation of pressure that travels through a solid, liquid, or gas in a wave pattern. These waves show different characteristics, including wavelength, frequency, period, and amplitude. Sound waves are described mathematically by the acoustic wave equation. In order to find the solution to the acoustic wave equation, some concepts should be discussed, such as the physical principles behind it and the way to characterize it.

Sound is a pressure wave that propagates through a fluid medium (a gas or a liquid) at a characteristic speed ($343 m/s$ in dry air at $20°C$). For this wave motion to take place, the medium has to possess inertia and elasticity. Sound waves are longitudinal waves characterized by adjacent compression and expansion regions. The fluid particles oscillate back and forth in the wave propagation direction (i.e., the particle velocity is in the same direction as the wave propagation speed), and consequent pressure fluctuations occur. Therefore sound waves produce energy transfer without any net mass transfer.

Sound pressure is the local pressure deviation from the ambient atmospheric pressure caused by a sound wave, simply it's the dynamic change in the fluid pressure about its equilibrium value, and usually, it's referred to as the fundamental acoustic variable.

2.2 Microfluidics and Perturbation Theory

Microfluidics deals with the flow of fluids and suspensions in channels of sub-millimeter-sized cross-sections under the influence of external forces. The downscaling leads to an increased surface-to-volume ratio. In the microdomain, surface tension and viscosity dominate over gravity and inertia, assuring the absence of turbulence and the appearance of regular and expected laminar flow streams, which indicates an exceptional spatial and temporal control of solutes.

Acoustofluidics, i.e., ultrasound-based external forcing of microparticles in microfluidics, has attracted particular attention because it provides gentle, label-free separation based on purely mechanical properties: size, shape, density, and compressibility (Laurell and Lenshof, 2014).

In the following, we use the so-called Eulerian picture of the continuum fields, where we observe how the fields evolve in time at each fixed spatial position (r). Consequently, the position (r) and the time (t) are independent variables. In general, the value of any field variable $F(r,t)$ is defined as the average value $\left\langle F_{mol}(r^{'},t)\right\rangle$ of the corresponding molecular quantity for all the molecules contained in some liquid particle of volume $\Delta V(r)$ around (r) at time (t)

$$F(r,t) = \left\langle F_{mol}(r^{'},t)\right\rangle_{r'\in\triangle V(r)} \tag{2.1}$$

If we, for brevity, let m_i and v_i be the mass and the velocity of molecule (i), respectively, and furthermore let $i \in \Delta v$ stands for all molecules (i) present inside the volume $\Delta v(r)$ at time (t), then the definition of the density $\rho(r,t)$ and the velocity field $v(r,t)$ can be written as

$$\rho(r,t) \equiv \frac{1}{\triangle v}\sum_{i\in\triangle v} m_i \qquad\qquad v(r,t) \equiv \frac{1}{\rho(r,t)\triangle V}\sum_{i\in\triangle v} m_i\, v_i \tag{2.2}$$

the velocity is defined through the more fundamental concept of momentum with the symbol " ≡ " to mean "equal by definition".

The dependant field variable in microfluidics can be scalars(such as density (ρ), viscosity (η), pressure (p), temperature (T), and free energy (ϕ)), vectors (such as velocity (v), current density (J), pressure gradient (Δp), force density (f), and electric field (E)), and tensors (such as stress tensor (σ) and velocity gradient (Δv))

2.2.1 Governing Equation

The mathematical treatment of microfluidic problems is complicated due to the presence of several scalars, vector and tensor fields, and the non-linear partial differential equations that govern them. To facilitate the treatment, a simplified notation is used (Bruus, 2008).

Simplidifed Notation:

- The suitable co-ordiante system is the Cartesian co-ordinate (x,y,z) with corresponding basis vectors e_x, e_y, and e_z of unity length and that are mutually orthogonal.
- Any vector (v) can be written in terms of it's components v_i (where for Cartesian co-ordinate $i = x,y,z$) as

$$v = \sum_{i=x,y,z} v_i e_i \equiv v_i e_i \tag{2.3}$$

- For the partial derivatives of a given function $F(r,t)$, we use the symbols (∂_i), with $i = x, y, z$, and (∂_t)

$$\partial_x F \equiv \frac{\partial F}{\partial x} \qquad \partial_t F \equiv \frac{\partial F}{\partial t} \tag{2.4}$$

- The vector differential operator nabla (∇) contains the three space derivatives ∂_i (Laurell and Lenshof, 2014). It is defined by

$$\nabla \equiv \partial_x^2 + \partial_y^2 + \partial_z^2 \tag{2.5}$$

- total time derivative expressed as

$$\frac{dF}{dt} = \partial_t F + (\partial_t r_i)\partial_i F = \partial_t F + (v \cdot \nabla)F \tag{2.6}$$

The Continuity Equation

The first governing equation is the continuity equation which express the conservation of mass

In many cases, especially in microfluidics, where the flow velocity is much smaller than the velocity of the speed of sound (pressure waves), the fluid appears in-compressible, and the continuity equation simplifies to

$$\nabla \cdot v = 0 \qquad or \qquad \partial_i v_i = 0 \tag{2.8}$$

The Navier-Stokes Equation

The second governing equation, the Navier–Stokes equation, is the equation of motion for the Eulerian velocity field directly related to momentum conservation and the momentum density (ρv).

Normally, for the so-called Newtonian fluids that the viscosity is independent of the shear rate and remains constant at a given temperature, the viscosity coefficients η and β can be taken as constants, and you can express the Navier-Stokes equation for compressible fluids as

$$\rho\left[\partial_t v + (v \cdot \nabla)v\right] = -\nabla p + \eta\nabla^2 v + \beta\eta\nabla(\nabla \cdot v) + \rho g \tag{2.9}$$

Volume viscosity disappears for incompressible fluids and the equation expressed as ($\nabla v = 0$), and the equation expressed as

$$\rho\left[\partial_t v + (v \cdot \nabla) v\right] = -\nabla p + \eta \nabla^2 v + \rho g \tag{2.10}$$

The Heat-transfer Equation

The third and last governing equation is the heat-transfer equation. The thermodynamic quantities for fluids are usually taken per unit mass, directly relating them to the fluid molecules. Thus, we work with the internal energy (ϵ) per unit mass, the entropy (s) per unit mass, and the volume ($1/\rho$) per unit mass instead of the energy (E), the entropy (S), and the volume ζ of the fluid. The first law of thermodynamics relates internal energy ($d\epsilon$), heat (Tds), and pressure work ($pd(1/\rho)$), and per unit mass it becomes

$$d\epsilon = Tds - pd\frac{1}{\rho} = Tds + \frac{p}{\rho^2} d\rho \tag{2.11}$$

In microfluidics, the fluid velocities are generally much smaller than the speed of sound in the fluid. Consequently, pressure variations are minute, leading to the constant pressure approximation, for which ($ds = c_p dT$), where (c_p) is the specific heat at constant pressure. In this case the heat-transfer equation is

$$\rho c_p\left[\partial_t T + v_j \partial_j T\right] = \partial_j\left(k \partial_j T\right) + \sigma'_{jk} \partial_k v_j \tag{2.12}$$

For a fluid at rest ($v_j = 0$) with a constant thermal conductivity (k), the equation reduces to the Fourier equation, which introduces the thermal diffusivity ($D_{th} = K/\rho c_p$)

$$\partial_j T = D_{th} \nabla^2 t \tag{2.13}$$

Table 2.1 – Typical Values for water at 20°C

Density	$\rho = 10^3 Kg/m^3$
Viscosity	$\eta = 10^{-3} Pas$
Coefficient for dilatational viscosity	$\beta = 3$
Heat conduction	$k = 0.6 W/mK$
Specific heat	$c_p = 4.2 \cdot 10^3 J/kgK$
Thermal diffusivity	$D_{th} = 1.43 \cdot 10^{-7} m^2/s$
Speed of sound	$c_0 = 1.5 \cdot 10^3 m/s$

2.2.2 Perturbation Theory

Ultrasound acoustics in the low MHz range is well suited for applications within microfluidics. For example, when frequencies $f \geq 1.5MHz$ are combined with the speed of sound in water at room temperature: $c_{wa} \approx 1.5 \times 103ms^{-1}$, the corresponding wavelengths $\lambda_{wa} \leq 1mm$ may fit into the submillimeter-sized channels and cavities in microfluidic systems and result in the formation of standing pressure waves known as resonance modes. For several reasons it is often advantageous to operate an acoustofluidic device at these resonance modes:

- They are usually both stable and reproducible.
- Their spatial patterns are controlled by the geometry of the microfluidic channel.
- At resonance, a maximum of acoustic power is delivered from the transducer to where it is needed in the system in the form of acoustic radiation force on suspended particles (Bruus, 2012).

In most cases of importance for acoustofluidics, the acoustic contributions to the pressure, density, and velocity fields can be considered as small perturbations. One systematic way of solving the equation of motion for acoustics is, therefore, to employ perturbation theory. As the unperturbed state, before applying any acoustic fields, we take a homogeneous liquid at rest in thermal equilibrium. Therefore The zero-order terms take the constant values

$$v_0 = 0 \qquad \rho_0 = \rho^* \qquad p_0 = p* \tag{2.14}$$

According to Kelvin's circulation theorem, which stated that if one observes a closed contour at one instant and follows the contour over time (by following the motion of all of its fluid elements), the circulation over the two locations of this contour is equal (Dolzhansky, 2013). The velocity potential can be introduced whenever viscosity is negligible, and this is a good approximation in the case of acoustofluidics. Following the convention of (Guo and Hong, 1993), we consider the velocity potential (ϕ) for ($\eta = 0$) as

$$v = \nabla\phi \qquad \frac{1}{\rho}(\partial_\rho p)_0(\rho - \rho_0) \approx -\partial\phi \tag{2.15}$$

The essential feature of acoustic waves in first-order perturbation theory for non-viscous fluids consists of the fundamental quantities as the velocity potential (ϕ), which to first order is written as ($\phi = \phi 1$). The related velocity, density, and pressure fields are given by Eqs 2.15

$$v = 0 + v_1 = \nabla\phi_1 \tag{2.16}$$

$$\rho = \rho_0 + \rho_1 = \rho_0 - \frac{\rho_0}{c_a^2}\partial_t\phi_1 \tag{2.17}$$

$$p = p_0 + p_1 = p_0 + c_a^2\rho_1 = p_0 - \rho_0\partial_t\phi_1 \tag{2.18}$$

while the corresponding first-order part of the continuity equation (**??**) and the Navier–Stokes equation (2.9) for zero viscosity are

$$\partial_t \rho_1 = -\rho_0 \nabla \cdot v_1 \tag{2.19}$$

$$\rho_0 \partial_t v_1 = -c_a^2 \nabla \rho_1 \tag{2.20}$$

One class of simple solutions to the wave equation are plane waves of constant amplitude (ϕ_0) propagating along a given constant the wavevector ($k = ke_k$) with angular frequency (ω)

$$\phi_1(r,t) = \phi_0 e^{i(k\cdot r - \omega t)} \tag{2.21}$$

If $\omega^2 = c_a^2 k^2$, or in other words the linear acoustic dispersion relation is fulfilled

$$\omega = c_a k \tag{2.22}$$

in terms of frequency ($f = w/(2\pi)$) and wavelength ($\lambda = 2\pi/k$) we have

$$f = c_a \frac{1}{\lambda} \tag{2.23}$$

Inserting this in the wave equation leads to the Helmholtz equation

$$\nabla^2 \phi_k(r) = -\frac{\omega^2}{c_a^2}\phi_k(r) = -k^2 \phi_k(r) \tag{2.24}$$

which is an eigenvalue problem that for given boundary conditions allows only certain values of the wavevector (k) or frequency (ω), and that results in the so-called eigenmodes or resonance modes ($\phi_k(r)$) (Bruus, 2008).
The acoustic waves carry energy, intensity and momentum. The total energy density (E_{ac}) associated with the sound wave can be divided into a kinetic and a potential energy density, (E_{kin}) and (E_{pot}), respectively

$$E_{ac} = E_{kin} + E_{pot} = \frac{1}{2}\rho_0 \left[(\nabla \phi)^2 + (\frac{1}{c_a}\partial_t \phi)^2 \right] \tag{2.25}$$

Considering non-viscous fluids, the acoustic waves are undamped, and the energy density must therefore fulfill a continuity equation

$$\partial_t E_{ac} = -\nabla \cdot J_E \tag{2.26}$$

This expression can be used to determine the acoustic energy current density (J_E), also known as the acoustic intensity (I_{ac}).

2.3 Ultrasonic Manipulation and Piezoelectricity

Ultrasonic manipulation is performed in a fluid volume. This volume is either partially manipulation in droplets or flow-through channels or fully bounded by solid bodies. Because the impedance of these solid boundaries is finite, a pressure field in the fluid will necessarily give rise to motion and deformations of the solid surrounding it. Therefore the modeling of these surroundings is important in order to understand the system as a whole. In particular, resonances and damping of the various modes encountered and used in the fluid are influenced by the neighboring materials, including the container, the transducers used to excite the acoustic modes, and possible glue layers that attach the transducer to the container.

2.3.1 Characteristic Impedances

The wave speeds of the primary and secondary waves are (c_1) and (c_2), respectively. These terms come from geophysics and result from the fact that ($c_1 > c_2$) and hence the primary wave arrives first. They are often abbreviated as P- and S-waves, respectively. For plane waves in isotropic materials, P-waves are longitudinal, while S-waves are transverse (Dual and Schwarz, 2012).

$$c_1^2 = \frac{\lambda+2\mu}{\rho} \qquad\qquad c_2^2 = \frac{\mu}{\rho} \tag{2.27}$$

The two types of waves for the isotropic material interfere and get reflected at boundaries and interfaces to yield the modes of vibrations of the system. It must be noted that, in general, a P-wave is reflected as both a P-wave and an S-wave. The same is true for an incident S-wave. At interfaces, a part of the energy is transmitted, another part is reflected depending on material properties and incident angle. The amount of energy that flows through an interface can strongly influence the amount of damping for a particular resonance mode in a micromanipulation device. For normal incidence, the reflected and transmitted energy flows R and T, respectively, divided by the incident energy flow, are given by

$$R = \frac{(Z_2-Z1)^2}{(Z_2+Z1)^2} \qquad\qquad T = \frac{4Z_1Z_2}{(Z_2+Z1)^2} \tag{2.28}$$

Where ($Z_i = \rho_i c_i$) are the characteristic impedances of the two materials. ($R + T = 1$) because of conservation of energy and both coefficients are independent of the direction of the energy flow. For the silicon water interface and normal incidence, ($R = 0.75$) and ($T = 0.25$). Even though a hard wall boundary condition is often assumed in simplified models, which would correspond to ($R = 1$), in reality, 25% of the incident energy flow will pass through the interface.

2.3.2 Piezoelectricity

Exciting and detecting motion in solids and fluids utilizing piezoelectric materials, in which an electric signal is converted into a mechanical motion and vice versa, has been used extensively

for ultrasonic particle manipulation. This method has several advantages:

- With the availability of programmable signal generators, waves of complex shape and frequency content can be produced with a high degree of repeatability, which opens the way to various signal processing techniques.
- By appropriately tailoring the transducer set-up, different waves and vibrations can be excited and measured selectively (Dual and Möller, 2012).

A necessary condition to make use of the above-mentioned advantages is the availability of materials with sufficiently high piezoelectric constants. Piezoelectric materials have been used in ultrasonic particle manipulation from the very beginning. Red blood cells were segregated using planar ultrasound transducers (Baker, 1972). Standing and traveling waves were used to manipulate cells for a number of applications (Coakley et al., 1989), and their acoustic energy can be focused by special non-planar transducers (Hertz, 1995) (Dual and Möller, 2014).

A typical transducer as used in the experimental setup is brought in contact with the structure to be excited using a coupling agent or glue. Classical ultrasonic transducers work in a resonant mode with defined frequency (resonance) at which they work best. When used in a continuous mode, one has to be careful not to heat up the transducer too much. This is particularly true for ceramic transducers. Heat is generated by the mechanical and electrical damping of the piezoelectric material.

2.4 Acoustic Radiation Forces

The force generated by an external acoustic field acting on bubbles, drops or particles, without considering the interaction between neighboring objects, is known as the primary acoustic force (Yosioka and Kawasima, 1955) (Gor'kov, 1962) calculated the acoustic radiation pressure on a compressible sphere giving rise to the primary acoustic force for plane standing waves. In the direction of propagation of the wave, this force is given by

$$F_z = 4\pi R^3 E_{ac} k G sin(2k_z) \tag{2.29}$$

where R is the radius, (E_{ac}) is the average acoustic energy density, (k) is the wavenumber, (z) is the distance from the nearest pressure antinode and (G) is the acoustic contrast factor defined as

$$G = 1 - \frac{\beta_p}{\beta_f} + \frac{3(\rho_p - \rho_f)}{2\rho_p + \rho_f} \tag{2.30}$$

Where (β) is the compressibility, (ρ) is the density, and subscripts (ρ) and (f) correspond to particle and fluid, respectively. For ($G < 0$) (generally the case of gas bubbles), particles move

to the pressure antinodes by the action of the primary acoustic force. However, if particles are denser than the surrounding fluid ($G > 0$), they are driven to the pressure nodes (Garcia-Sabaté et al., 2014).

When two bubbles approach each other, they seem to suddenly increase their relative velocity and coalesce to form a larger single bubble. If the coalescence continues, the bubble soon exceeds resonance size and it is propelled away from the antinode, often leaving small bubbles along its track, which are drawn toward the antinode, recoalesce, and so forth.

The various forces on an air bubble in a sound field are often referred to as Bjerknes forces after C. A. Bjerknes and his son V. F. K. Bjerknes, who was the first to report on such forces (Bjerknes, 1906).

There appear to be two general classes of Bjerknes forces; the attraction or repulsion of individual air bubbles by the pressure antinode of a stationary sound field is one type, and the mutual attraction or repulsion of air bubble is a second type. It should be understood that there exists only one force here the acoustic radiation-pressure force of a sound field on a local inhomogeneity. The mutual attraction or repulsion results from the secondary radiated sound fields of the pulsating bubbles caused by the action of the primary sound field upon the individual bubbles. The force exerted on an air bubble due to the primary sound field is called the primary Bjerknes force, and the force between two air bubbles due to the secondary sound fields radiated by the bubbles are called the secondary or mutual Bjerknes force between air bubbles (Crum, 1975).

2.4.1 The Bjerknes Forces

The forces proposed by the two Bjerknes Were based upon the law of kinematic buoyancy and are analogous to the Archimedes law. Bjerknes proposed that "anybody which participates in the translatory motion of a fluid is subject to a kinetic buoyancy equal to the product of the acceleration of the translatory motion multiplied by the mass of water displaced by the body. The position of a particle of an oscillating fluid can be represented by

$$\xi(t) = \xi_0 + \xi_1 sin(\omega t) \qquad M(t) = \rho V(t). \tag{2.31}$$

Where (ξ_0) is the mean position, (ξ_1) is its maximum displacement, and M is the mass of the fluid. If the Bjerknes statement is applied directly and expressed in terms of acoustic pressure ($p_a(r,t)$) rather than the particle velocity

$$\rho \frac{\partial u(t)}{\partial t} = -\nabla p_a(r,t) \tag{2.32}$$

A more commonly used form is the time-averaged Bjerknes force expressed as

$$F_B^{'} = -\left\langle V(t)\nabla p_a(r,t)\right\rangle \tag{2.33}$$

This is the expression for the Bjerknes force on an air bubble due to the pressure gradient of the primary sound field.

Suppose that two pulsating bubbles are separated by a distance (r), which is sufficiently great that the pressure generated by bubble one at the location of bubble two is essentially that which would result if bubble two did not exist. The primary sound field which causes the bubble to pulsate is much larger than the secondary sound fields, which cause the bubbles to be attracted toward each other. Consequently, the second-order effect of the bubbles interfering with each other's radiation field.

$$R_1(t) = \overline{R}_1 + \delta_1 sin(\omega t) \tag{2.34}$$

Where (R_1) is the radius of bubble 1, ($\overline{R}_1$) is the mean radius and (δ) is the pulsation amplitude. A similar expression applies to bubble 2. The pressure field radiated by bubble 1 at the site of bubble 2 is given approximately by

$$p(r,t) = -(\rho\overline{R}^2/r)\omega_{2]}\delta_1 sin(\omega t) \tag{2.35}$$

For small pulsations, the volume of bubble 2 can be expressed as

$$V_2(t) = \tfrac{4}{3}\pi\overline{R}_2^3\delta_2 sin(\omega t + \phi) \tag{2.36}$$

where (ϕ) is the phase angle between ($R_1(t)$) and ($R_2(t)$). Thus, the Bjerknes force between two bubbles of mean radii ($\overline{R_1}$)and ($\overline{R_2}$) with respective pulsation amplitudes (δ1and δ_2) separated by some distance (r), is given by

$$F_B = 2\pi\rho\omega^2\delta_1\overline{R}_2^1\overline{R}_2^2 cos(\phi)(r/) \tag{2.37}$$

If the pulsations are in phase, the force is negative, which implies attraction (Crum, 1975).

2.4.2 The drag on the bubbles

It is known that the drag force on most bodies moving through fluids cannot be predicted analytically except at very small Reynolds number. The Reynolds number for a body moving through a fluid is a dimensionless number defined by ($R_e = \rho Du/\mu$), where (ρ) is the density and (μ) the dynamic viscosity of the fluid, (D) the diameter, and (u) the magnitude of the

velocity of the body.

The drag force on a rigid sphere can be expressed by Stokes's law only for Reynolds numbers less than 1.0.

The drag force on a body of cross-sectional area (A), moving with velocity (u) through a fluid of density (ρ), is normally expressed as

$$F_D = -\frac{1}{2}\rho u^2 A C_D \hat{u} \tag{2.38}$$

where (C_D) is the drag coefficient and ($\hat{u}$) is a unit vector in the direction of (u) (Crum, 1975).

3 Experimental setup

3.1 System Description

3.1.1 Matlab System Diagram

The system consists of an ultrasonic driving module and control equipment. Figure 3.2 shows a detailed flowchart of the system for the whole experiment. The driving modules are ultrasonic transducers attached to a microfluidic channel, which contains the micro/nano-robots. The

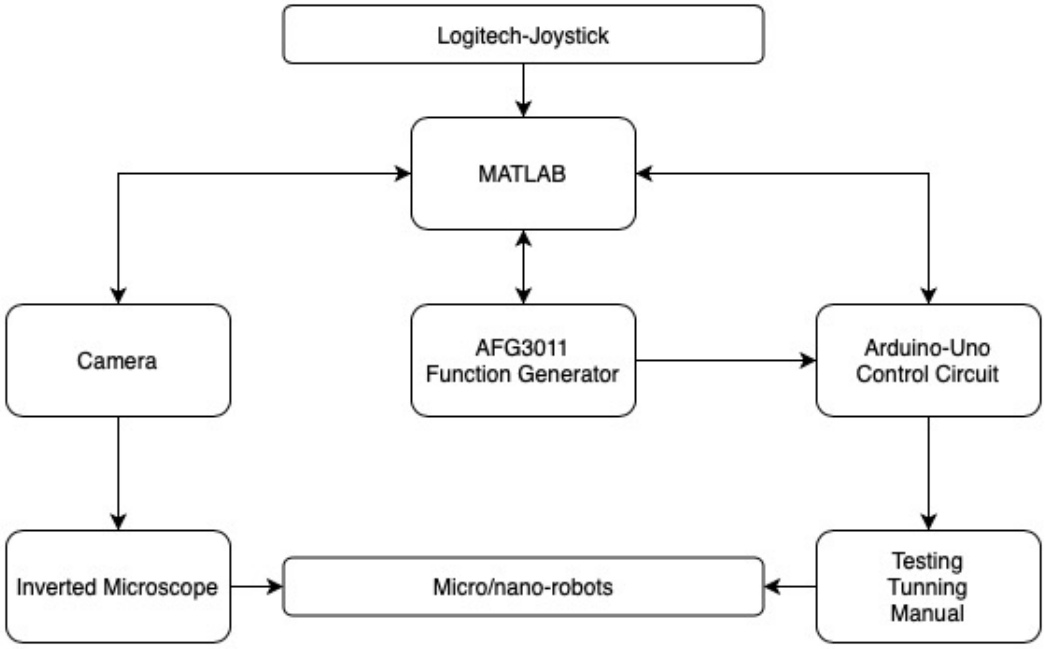

Figure 3.1 – Matlab System diagram

ultrasonic transducer used has a resonant frequency of 242 kHz. The control unit consists of a

function generator (Tektronix AFG31000) and a micro-controller (Arduino-Uno). The input signal is a sinusoidal wave generated by the function generator and transmitted through the switching control circuit controlled by the micro-controller. The frequency, amplitude, and micro-controller are controlled through Matlab, which receives the command from the joystick. In addition, the camera (Hamamatsu C11440) was connected to an inverted microscope to capture live images and send them to Matlab to process and use them as feedback for the tunning mode.

3.1.2 Python System Diagram

The main difference between the first diagram is that using python, we were able to capture and process 50 frames per second from the camera, which allowed the feedback control to track the micro/nano-robots and move them autonomously in the microfluidic channel. In addition, instead of using the joystick, we used the keyboard buttons as an input for testing the Piezo transducer, which allowed the system to cut the interface time between the joystick and to be more portable.

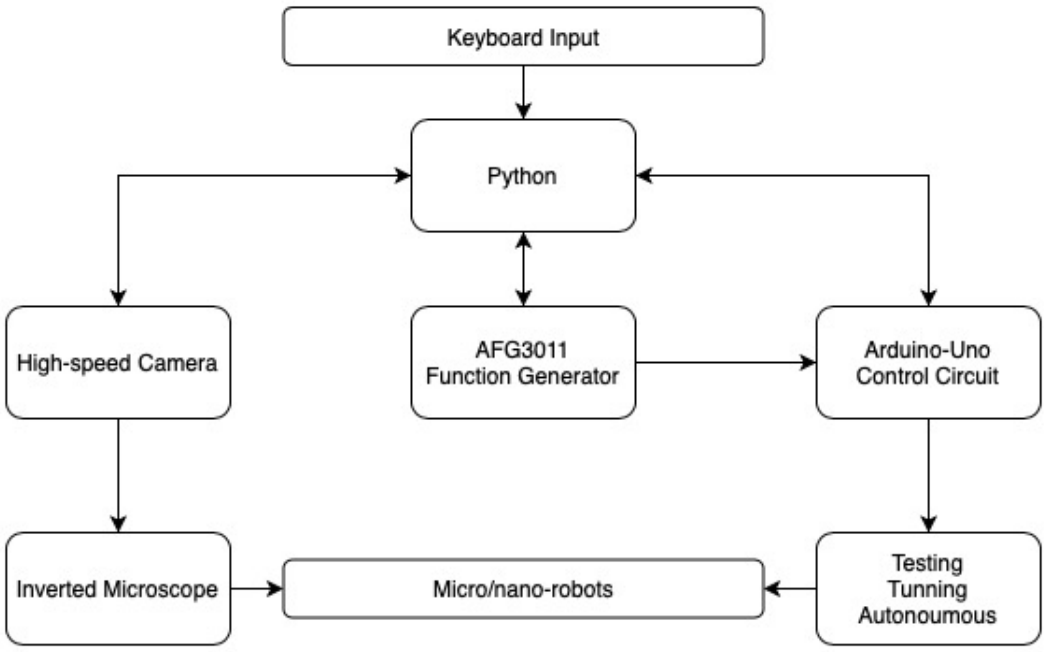

Figure 3.2 – Python System diagram

3.2 Microfluidic Channel

Microfluidic channels were fabricated with polydimethylsiloxane (PDMS) using standard soft lithography. Each device was fabricated using a master mold, lithographically patterned

with SU-8 negative photoresist on a 4-inch silicon wafer, later placed inside a Petri dish. Commercial thermocurable PDMS prepolymer was prepared by mixing the base and curing agent at a 10:1 weight ratio, following which the PDMS prepolymers were degassed under vacuum and cast onto the mold. Thermal cross-linking of PDMS was performed by curing at 80 °C for two hours. The cured PDMS was cut and peeled off from the channel mold, following which the inlet and outlet access ports were created by using a 1 -mm-diameter punch. Next, the PDMS channel was bonded with another layer of PDMS under 80 °C for two hours. Experiments were conducted after plasma pretreatment for 1 min. Three different channels have been used to capture how the micro-bubbles behave; every channel shows a different obstacle for micro-bubbles manipulation.

3.2.1 Square Channel with 4 piezos

The first experiment was done on a square channel with a $400 \times 30 \mu m$ cross-section to observe the behavior of the environment by actuating every piezo transducer separately. When the micro-bubbles cluster together and move close to the wall, they stick to the wall, which is helpful for the application, so starting with a $400 \mu m$ channel gave more space to see how the bubbles, particles behave far away from the wall.

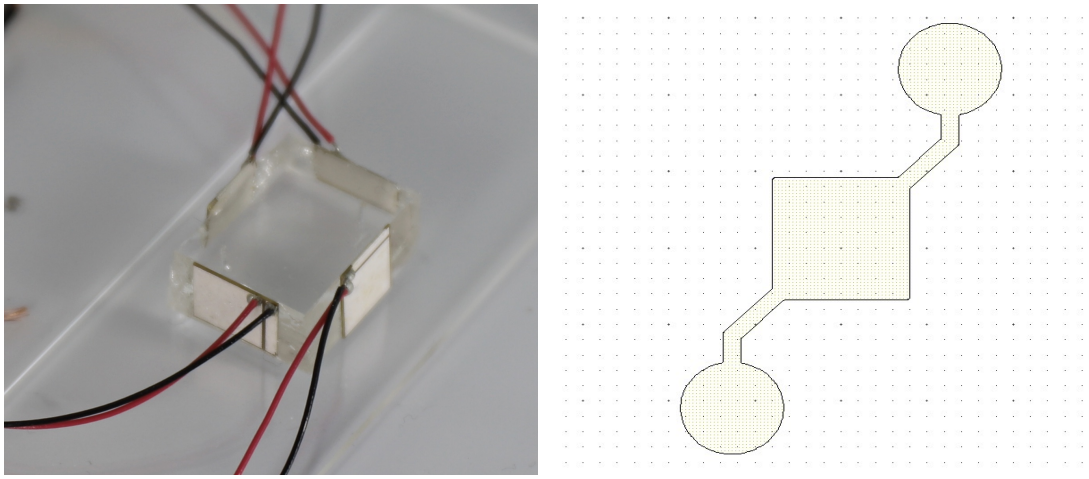

(a) PDMS channel (b) Channel Design

Figure 3.3 – Square-channel with 4 piezos

3.2.2 Simple channel with 6 piezos

The concept for using six transducers is to try to mimic an actual life application, especially in vivo application; for example, applying an acoustic pressure to be perpendicular to the cross-section of a vein in the human body is not realistic. Using two transducers angeled with 30 degrees with respect to the channel and exciting them together at the resonant frequency act as one piezo-transducer perpendicular to the cross-section of the microfluidic channel.

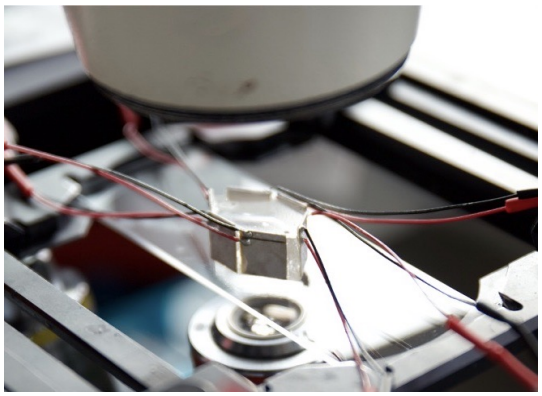

(a) PDMS channel

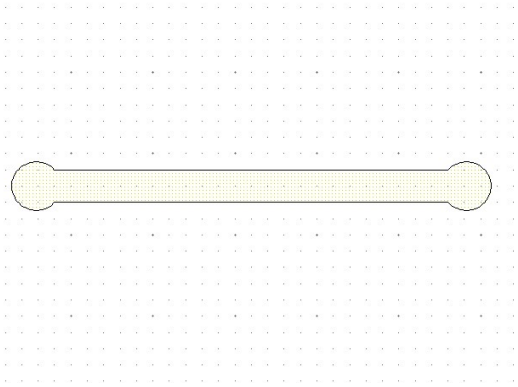

(b) Channel Design

Figure 3.4 – Simple-channel with 6 piezos

3.2.3 Bifurcation Channel with 4 piezos

Micro/nano-robots have the potential to create new opportunities in targeted and precise drug delivery. Acoustics with the ability to generate forces wirelessly will make existing therapeutic and diagnostic procedures less invasive and enable new methods never before possible. For example, controlling the microrobots in a chaotic flow environment, as we find in the carotid arteries in the human body, is an important phenomenon to investigate.

The carotid arteries are the blood vessels that carry oxygen-rich blood to the head, brain, and face. They exist on each side of the neck. The human carotid artery consists of the common carotid artery (CCA) that bifurcates into the external carotid artery (ECA) and internal carotid artery (ICA) (Urschel et al., 2021). In this channel design, the idea is not only to mimic the shape of the veins in vivo but also to study the chaotic flow as represented in Figure 3.5 (d) in the channel when the atherosclerotic plaque exists.

While designing the channel, the carotid arteries model dimensions have been taken from the literature (Nagargoje and Gupta, 2020). The diameter of the main artery as represented in Figure 3.5 (c) is 8mm, and the bifurcation is 4.6 mm and 5.5 mm with an angle of 50 degrees with downscaling five times to implement it on a small chip.

The questions here were how this chaotic flow affects the acoustic pressure and the bubble clustering and how we can manipulate the bubbles or particles inside this flow, which will help to have a better drug delivery and reach points where the drugs were not able to reach.

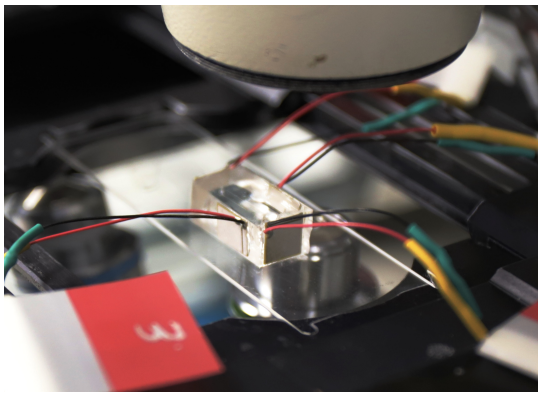

(a) PDMS channel

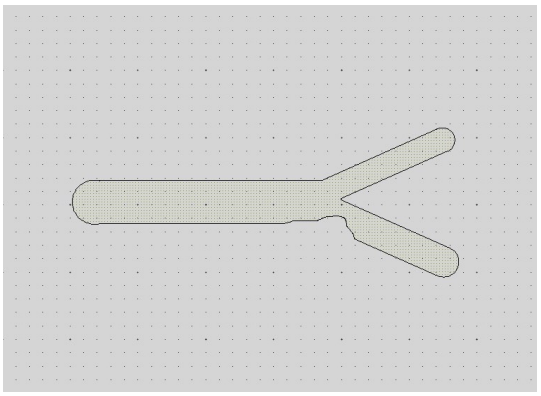

(b) Channel Design

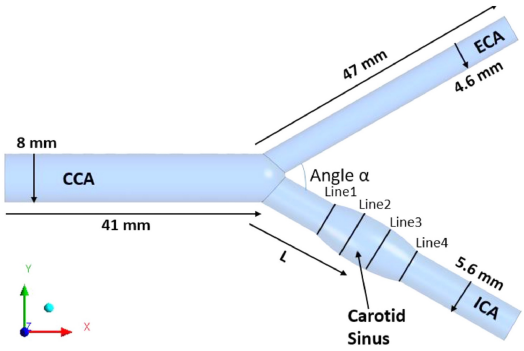

(b)

(c) Arterial Bifurcations channel dimensions (Nagargoje and Gupta, 2020)

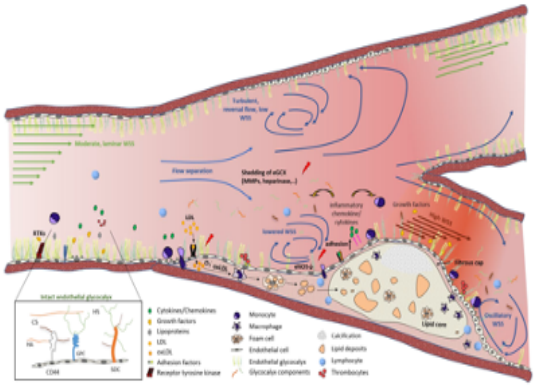

(d) Arterial bifurcations channel in vivo (Urschel et al., 2021)

Figure 3.5 – Arterial bifurcations channel.

3.2.4 Chaotic Flow Channels

The design of the carotid artery had a chaotic flow behavior. However, to observe it, we needed to reach a high fluid velocity which made controlling the microrobots not possible anymore.

Investigation of new designs was needed to study the behavior of microrobots in a chaotic flow with lower velocities. We can capture the flow profile with 50 framers per second and by designing new microfluidic channels that have arbitrary shapes and cavities in addition to observing the idea of mimicking arteries and aneurysms in the human body.

As represented in the Figures3.6 below, 18 channels have been designed to study the flow profile. The material for the channels is PDMS, which has been the most widely used material for the applications of soft lithography because of its useful properties, including low cost, biocompatibility, low toxicity, chemical inertness, versatile surface chemistry insulating, as well as mechanical flexibility and durability, the PDMS can also be easily manipulated and making PDMS devices can require very few equipments.

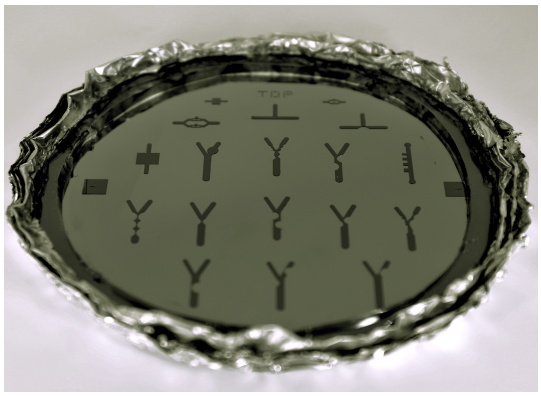

(a) Wafer design

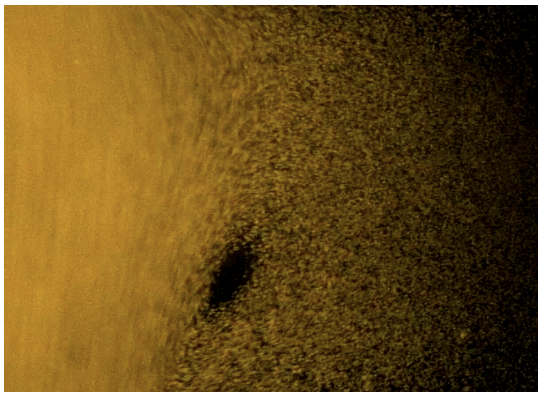

(b) Cavity channel

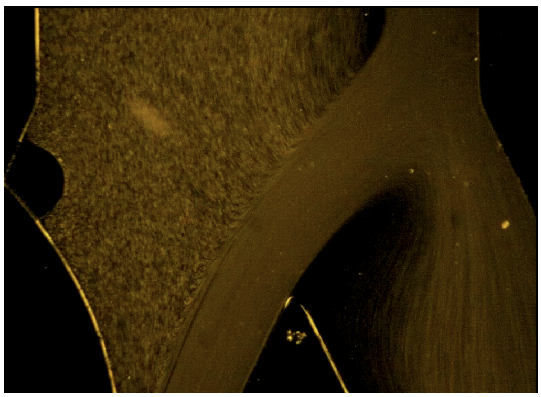

(c) Bifurcations channel

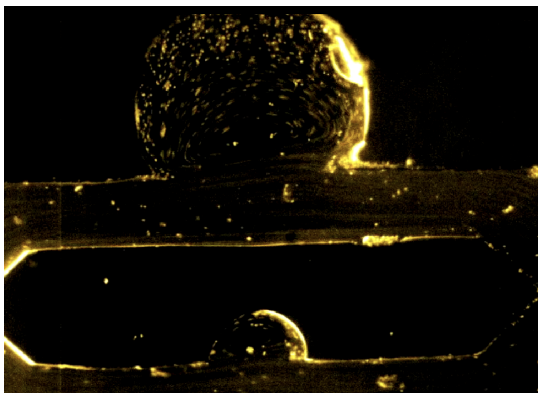

(d) Aneurysms channel

Figure 3.6 – Chaotic flow channel.

3.3 Microscope Setup

The piezo transducers were glued to the PDMS wall by using two-component epoxy glue. However, considering the animal trials, it's not feasible to glue the piezo to the skin, so a 3D printed mold has been designed and printed to hold the piezo transducers. Moreover, to guarantee the coupling, an ultrasound gel has been used between the holder and the piezo transducer

The material used for the holder is smooth Ecoflex (00-10 Platinum Cure silicone rubber); it is versatile and easy to use, Low viscosity makes mixing and deaerating easy. The Cured rubber is soft, strong, and very elastic, expands many times its original size without tearing, and returns to its original shape without distortion. Ecoflex rubbers are water-white, translucent as shown in Figure 3.7.

The holder design was meant to be placed on a mouse head with a hole in the middle to observe the mouse skull and the dimensions have been approximately taken by collaborating with the university hospital of Zurich.

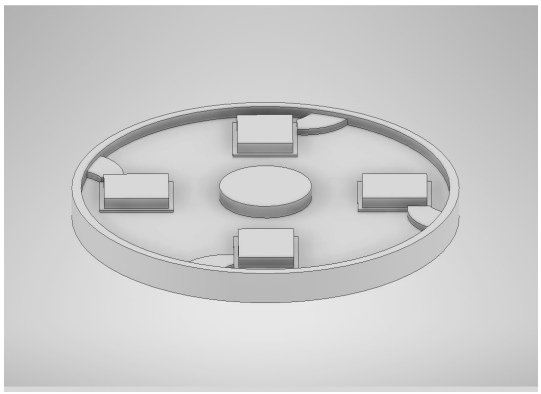

(a) Inventor Design

(b) 3D printed mold

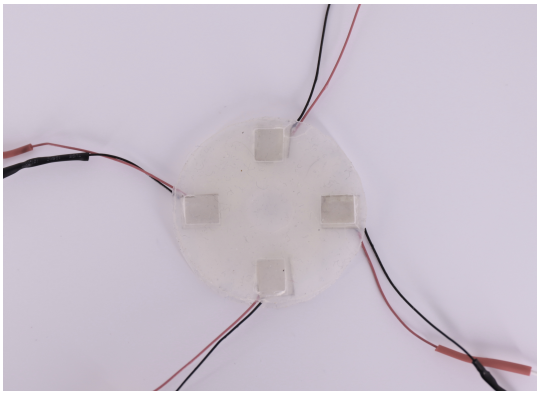

(c) Echo flex holder with 4 pizos

Figure 3.7 – Piezo transducer housing

3.4 Function generator

A function generator is electronic test equipment to generate different electrical waveforms over a wide range of frequencies. Some of the most common waveforms produced by the function generator are the sine wave, square wave, triangular wave, and sawtooth shapes. These waveforms can be either repetitive or single-shot. The wave generated by the function generator is an AC signal with high frequency and amplitude. Therefore, in order to control the circuit with a micro-controller, specific components will be required to isolate the circuit. In acoustics, a high-pressure force is required, which exists in the resonance frequency of each piezo transducer. Considering that even the same type of piezo-transducers might not have the same resonant frequency, it is essential to have more than one function generator to actuate more than one piezo-transducer simultaneously.

3.4.1 AFG31000 Series Arbitrary Function Generator

Generate waveforms with fine timing resolution. Up to 20 Vp-p amplitude into 50Ω load. The interface and control have been done on the AFG using MATLAB and instrumental control toolbox.

3.4.2 AD9850 or AD9833

The AD9850 is a highly integrated device that uses advanced DDS technology coupled with a high internal speed, high-performance D/A converter, and comparator to form a complete, digitally programmable frequency synthesizer and clock generator function. The AD9850 generates a spectrally pure, frequency/phase programmable, analog output sine wave when referenced to an accurate clock source. This sine wave can be used directly as a frequency source. The output voltage from this DAC is not enough to act as a good acoustic pressure source so, HF-Voltage-Amplifier has been used to amplify the output, the input for the amplifier is from 1-4 volt, and the corresponding output is multiplied by 7, which allowed to reach to 30 volts.

3.4.3 XR-2206

The XR-2206 is a monolithic function generator integrated circuit capable of producing high-quality sine, square, triangle, ramp, and pulse waveforms of high stability and accuracy. The output waveforms can be both amplitude and frequency modulated by an external voltage. The frequency of operation can be selected externally over a range of 0.01Hz to more than 1MHz. The same HF-Voltage-Amplifier has been used to amplify the amplitude.

3.5 Control Circuits

The control circuit is crucial to control the system from the micro-controller and isolate the AC signals coming from the function generator with the electronic components that require a DC voltage. Two control circuits have been used to isolate and control the system.

3.5.1 Optocouplers and Triacs

The optocoupler is a device that works like a switch, connecting two isolated circuits on your PCB. When current stops flowing through the LED, the photosensitive device also stops conducting and turns off. All of this switching happens through a void of glass, plastic, or air with no electrical parts between the LED or photosensitive device. It's all about the light. Optocouplers can either be used on their own as a switching device or used with other electronic devices to provide isolation between low and high-voltage circuits.
The traic-optocoupler This type of optocoupler configuration forms the basis of a very simple

solid state relay application that can be used to control any AC mains-powered load such as lamps and motors. Also, unlike a thyristor (SCR), a triac is capable of conducting in both halves of the mains AC cycle with zero-crossing detection allowing the load to receive full power without the heavy inrush currents when switching inductive loads.

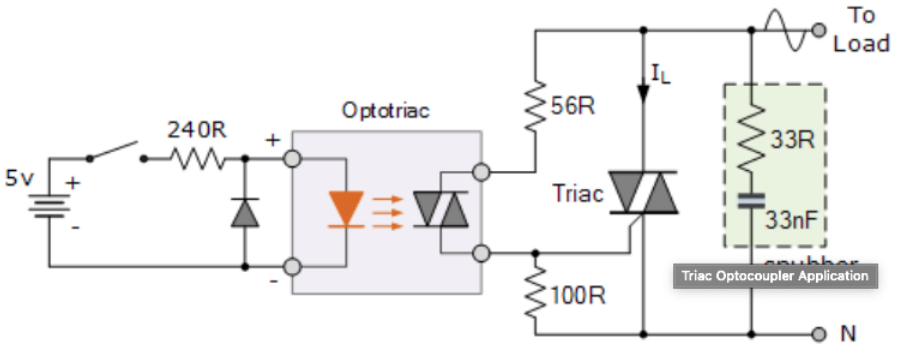

Figure 3.8 – electronics circuit with Optocoupler and Triac

MOC3063y or MOC3043

The MOC3063 and MOC3043 M devices consist of a GaAs infrared emitting diode optically coupled to a monolithic silicon detector performing the function of a zero voltage crossing bilateral triac driver. They are designed for use with a triac to power highvoltage circuits.

BT137-600D Triac

Planar passivated a very sensitive gate four quadrant triac in a SOT78 plastic package intended for general-purpose bidirectional switching and phase control applications, where high sensitivity is required in all four quadrants. This very sensitive gate "series D". triac is intended to be interfaced directly to microcontrollers, logic integrated circuits and other low power gate trigger circuits.

The switching time of the optocouplers and triacs is faster than the relay, but when you turn on the triacs, it leaks currents because of the high frequency and to stop the leaking, you need to turn on another signal to turn the triac off.

The circuit represented in Figure 3.9 has been built to suit the case of using six piezo transducers; it consists of six triacs, six optocouplers, a joystick to send signals to choose among the transducers which one should be on, and an Arduino-Uno microcontroller to send the digital signal to the optocouplers, which is connected to one pin of the triac to act as a switch for the sinusoidal wave coming from the function generator. The AC signal coming from the function generator is connected to the other pin of the triac and it's an isolated circuit, so all the negative AC pins are connected and the same for the negative microcontroller pins, but

there is no common ground between the negative of the microcontroller and the function generator.

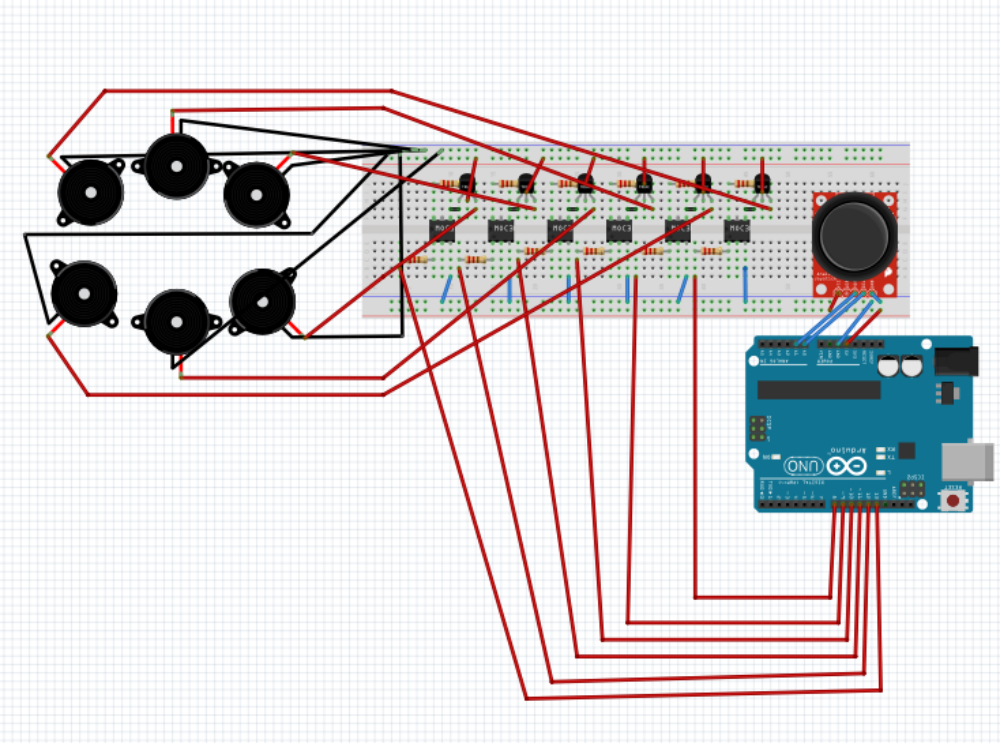

Figure 3.9 – Control circuit with Optocouplers and Triacs

3.5.2 DC Power Relay

A relay is an electromagnet with an internal spring-loaded lever to switch electrical contacts. A DC relay uses a single coil of wire wound around the iron core to make the electromagnet. When the DC coil is energized, the magnetism generated in the core is steady because the DC just keeps going. The steady magnetism keeps the lever attracted as long as the DC is flowing. Once the current is turned off and the iron core is no longer magnetized, the spring-loaded lever returns to a relaxed position, and the electrical contacts are switched back.

The relay time to turn on/off is from 5 to 15 ms. So it's slower than the other circuits. Still, it has the benefit of not leaking any current since, in the meantime, the bottle nick is coming from the feedback system with the image processing, which takes more than 1 second, so using the DC relay, in this case, is more feasible.

The schematic represented in Figure 3.10 is slightly different from the schematic before in Figure 3.9 . Here we refer to the four piezo transducers circuit with replacing the optocouplers and triacs with the electromagnetics relays.

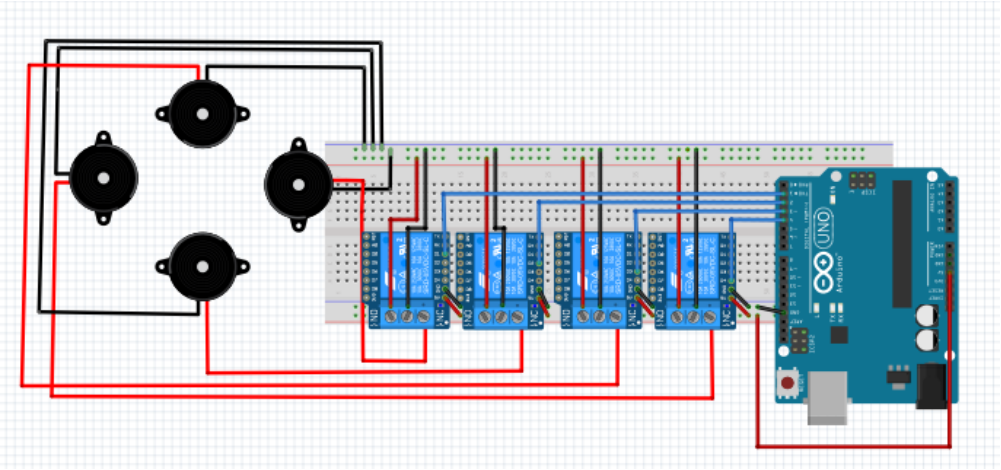

Figure 3.10 – Relays control circuit

3.6 Camera

3.6.1 Hamamatsu (C14041)

The C14040 as shown in Figure (3.11(a)) is an InGaAs camera with sensitivity in the near-infrared region from 950 nm to 1700 nm. It has a USB 3.0 interface port that supports 14-bit image acquisition and exposure time adjustment. The C14040 camera can capture a frame rate of approximately (216) frames per second. It has been used for the manual and autonomous mode with 50 frames per second.

3.6.2 Chronos (1.4)

The Chronos 1.4 high-speed camera as shown in Figure 3.11(b) is useful for operations that require relatively high frame rates for review and analysis. The high-speed camera has been used to capture the flow profile with a higher velocity to observe the chaotic flow behavior in the microfluidic channels.It captures a resolution of (1280x1024) @ (1069) frames per second and up to (40413) fps at lower resolution.

(a) Hamamatsu (C14041) camera (b) Chronos (1.4) camera

Figure 3.11 – Cameras.

4 Image Processing

Image processing uses algorithms and codes to analyze, interpret and extract information from the images. It has applications related to many fields, such as robotics, industry, and medical diagnosis.

Theoretically, a binary image is the simplest form of an image; it is a two-dimensional function that maps a coordinate pair to an integer value, which is related to the intensity of the point. Each point is called a pixel. An image can have multiple channels, too (for example, colored RGB images, where color can be represented using three channels (red, green, and blue). For a colored RGB image, each pixel at the (x,y) coordinate can be represented by a three-tuple (rx,y, gx,y, bx,y).

In order to be able to process it on a computer, an image f(x,y) needs to be digitalized both spatially and in amplitude. Digitization of the spatial coordinates (x,y) is called image sampling. Amplitude digitization is called gray-level quantization. In a computer, a pixel value corresponding to a channel is generally represented as an integer value between (0-255) or a floating-point value between (0-1). An image is stored as a file, and there can be many different types (formats) of files. Each file generally has some metadata and some data that can be extracted as multi-dimensional arrays (for example, 2-D arrays for binary or gray-level images and 3D arrays for RGB and YUV colored images) (Dey, 2018).

In this Chapter, The focus is on processing and extracting image data. Although Matlab is a powerful tool for image processing since it efficiently deals with matrices, it is still not an open source for everyone. In the first part, we used Matlab for image acquisition and processing, but the speed of processing the images was not fast enough to act as feedback for the system, then we used python with OpenCV since it's an open software and made it possible to process 50 frames per second which were fast enough for the feedback control.

4.1 Image Processing Pipeline

1. **Acquisition and storage**

   The image needs to be captured using a camera and stored on some device as a file (for example, a JPEG file).

2. **Load into memory and save to disk**

   The image needs to be read from the disk into memory and stored using some data structure in the case of using Matlab since the code is split into two parts, one for the acquisition and the other to access the images to process it. On the other hand, in the case of using python no need to save the pictures unless some data is needed for learning or showing.

3. **Manipulation, enhancement, and restoration**

   Run a few transformations on the image (sampling and manipulation; for example, grayscale conversion), then enhance the quality of the image (filtering; for example, deblurring) and restore the image from noise degradation

4. **Segmentation**

   The image needs to be segmented in order to extract the objects of interest.

5. **Information extraction/representation**

   The image needs to be represented in some alternative form; for example, one of the following

   - Some hand-crafted feature-descriptor can be computed (for example, edges,corners) from the image
   - Some features can be automatically learned from the image (for example, the weights and bias values learned in the hidden layers of a neural net with deep learning

6. **Image understanding/interpretation**

   This representation will be used to understand the image better with the following:

   - Image classification: is the image have micro-bubbles and does it have a useful information.
   - Object recognition:for example,finding the location of the micro-bubbles and the boundaries of the channel(Dey, 2018).

4.2 Image Processing Implementation

The image processing target is to detect the microbubbles clusters and segment them from the background flow. Keep in mind that the bubbles have shadows, and it is expected that there are specks of dirt inside the channel, which should not be identified as a swarm.

The Matlab code has been split into two parts running in parallel by using a parallel computing toolbox. The acquisition has been done by Hamamatsu Image Acquisition toolbox with a custom-made driver to suit the specific model of the camera.

4.2.1 Original Image

The original image is represented in Figure 4.1 has been imported from the same directory of the image acquisition. The image is for the microfluidic channel with 1 mm width and 15 mm length.

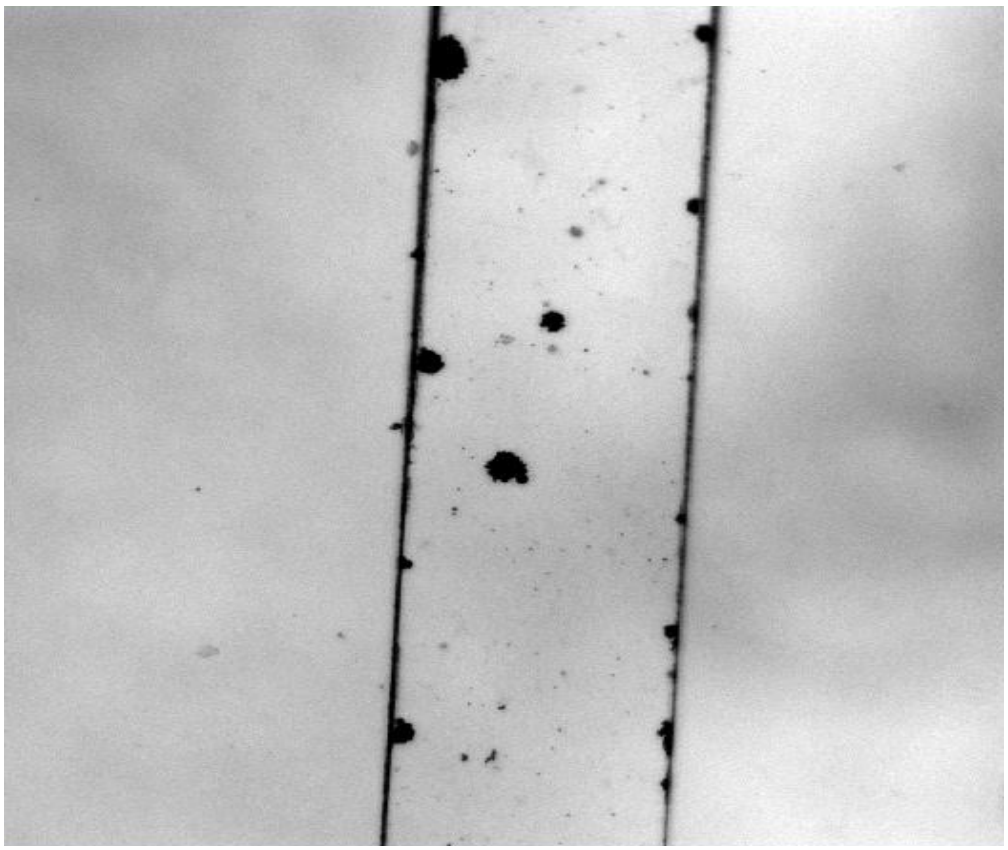

Figure 4.1 – Microfluidic channel with clustered microtobots

4.2.2 Edge Detection

The edge detection function takes an intensity or a binary image as its input and returns a binary image of the same size. The output matrix contains 0's and 1's with 1's where the function finds edges and 0's elsewhere.

The process of edge detection significantly reduces the amount of data and filters out unneeded information, while preserving the important structural properties of an image.

Edge detection function support six different edge-finding methods; the one is used here is the Sobel method as represented in Figure 4.2 (a), it works by calculating the gradient of image intensity at each pixel within the image. It finds the direction of the largest increase from light to dark and the rate of change in that direction. The result shows how abruptly or smoothly the image changes at each pixel, and therefore how likely it is that that pixel represents an edge (Gao et al., 2010).

4.2.3 K-means Clustering

K-means clustering is a type of unsupervised learning algorithm, which is used here to label the data and to segment the interest area from the background. K different random points were initiated in the data and assigned to the nearest centroid. After every point has been assigned, the centroid is moved to the average of all points assigned. Then the process repeats: every point is assigned to its nearest centroid, centroids are moved to the average of points assigned to it. The algorithm is done when no point changes the assigned centroid (Hartigan and Wong, 1979). The input for the algorithm is a binary image, and the target is classifying the bubbles and the boundaries of the channel as a cluster and the background as the other cluster as represented in Figure 4.2 (b).

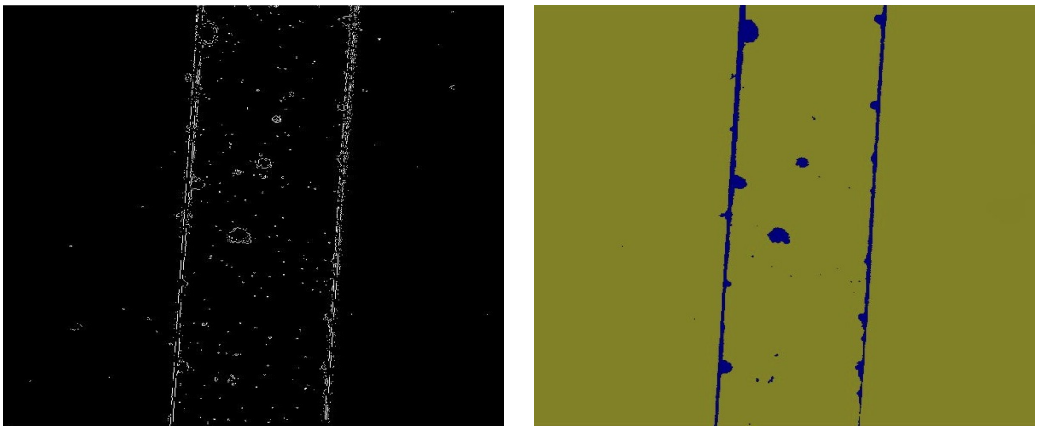

(a) Edge-detection (b) k-means-clustering

Figure 4.2 – Image processing first part

4.2.4 Identify Index Matrix

The resulting matrix coming from the K-means clustering is a combination of ones and twos; since K-means it is an iterative approach, sometimes the microbubbles might turn to number two and the background to number one.The solution is to identify the index matrix by checking which number is dominant in the resulting matrix and labeling it with zero and one for the others. The output is labeled binary image with ones for the microbubbles and zero for the background as represented in Figure 4.3 (a).

4.2.5 Morphological Operation

The most basic morphological operations are dilation and erosion. Dilation adds pixels to the borders of objects in an image, which makes objects more visible and fills small holes in objects, while erosion removes pixels on object borders, which removes islands and small objects so that only substantive objects remain. The number of pixels added or removed from the objects in an image depends on the size and shape of the structuring element used to process it.

Closing operation dilates an image then erodes the dilated image by using the same structuring element for both operations; as represented in Figure 4.3 (b), we used a disc element with 13 pixels diameter, which tunned to preserve the shape and size of the microbubble clusters and filled the small holes inside them.

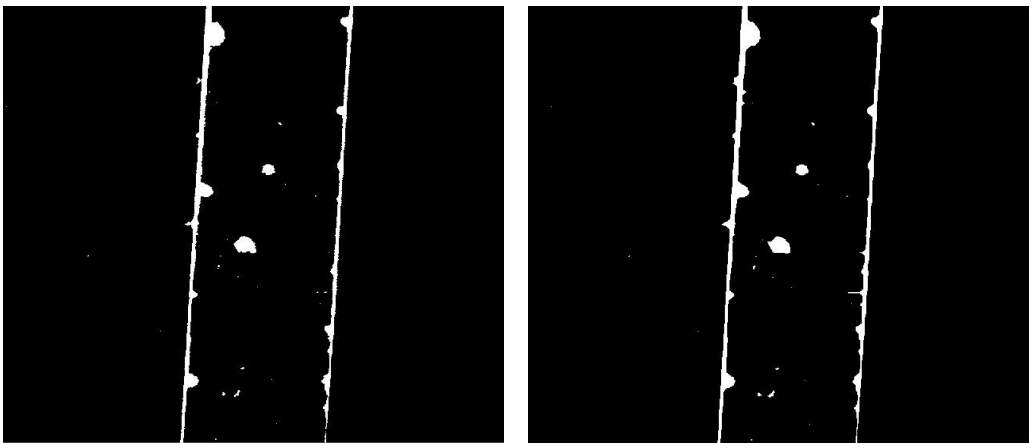

(a) black and white (b) Closed entities

Figure 4.3 – Image processing second part

4.2.6 Color-map

The color map is used to convert the closed entities image to the RGB matrix, which contains the connected component, so every closed entity will have a different color. The labeled RGB

images facilitate and speed measuring the image properties as represented in Figure4.4(a).

4.2.7 Filtering

The fabrication of microfluidic channels does not guarantee a clean channel without any specks of dirt. Moreover, the target is the largest cluster, so filtering the small clustered and the dirt helped increase the efficiency of the feedback control.

Removing the small clusters of air bubbles under a specific threshold with binary-area-open function eliminates all clustered bubbles with fewer than a specified pixels threshold, creating another binary image free of the small clusters as represented in Figure4.4(b).

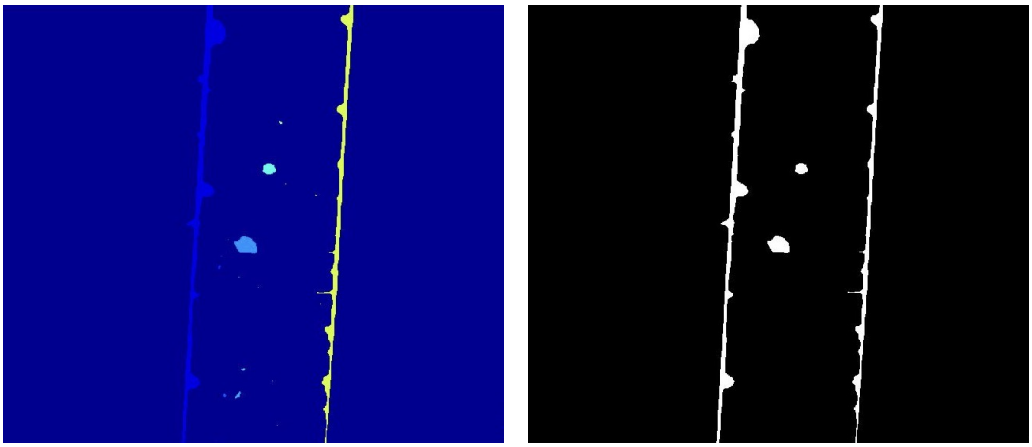

(a) Color map (b) Filtered image

Figure 4.4 – Image processing second part

4.2.8 Extract features

In order to extract the features of the microbubbles in the image, the region properties function has been used to measure a set of properties for each labeled region in the image. The most interesting properties are the area to target the largest clusters, perimeter to distinguish between the biggest cluster and the wall of the channel, and intensity to make sure the microscope is still in focus all the time. The output image separated the clusters with a unique ID independently as represented in Figure 4.4 (a)

4.2.9 Final Image

Finally, we extract the information from the picture and highlight our targets, which are the largest area for the clustered microrobots. We label the center of the cluster to be used in the tracking and save distances to the wall in the microfluidic channel, as represented in Figure 4.6 (b).

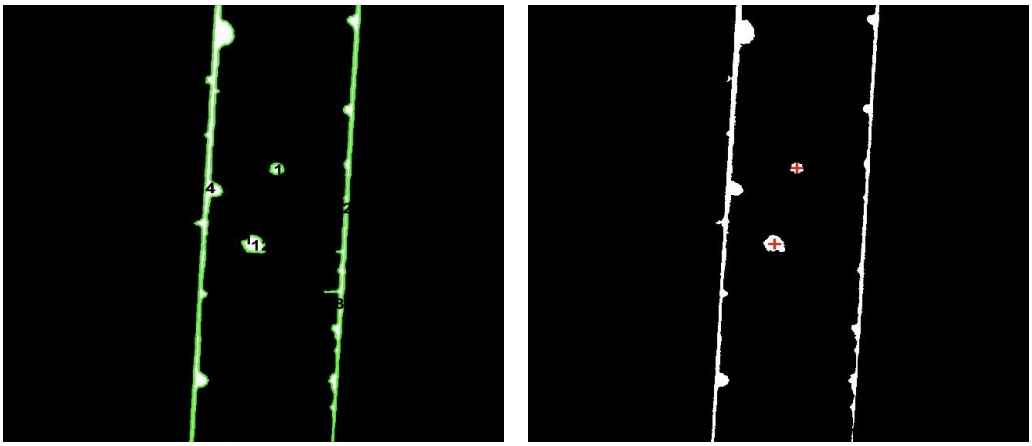

(a) Areas and Intensities (b) Final image

Figure 4.5 – Image processing fourth part

4.3 Image Processing with Python

The main difference between Matlab and python is that with using python, we were able to capture and process 50 frames per second from the camera, which allowed the feedback control to track the micro/nano-robots and move them autonomously in the microfluidic channel. In addition, python is free software, so the code becomes an open-source for everyone.

4.3.1 Object Detection

Object detection is a computer vision technique that allows us to identify and locate objects in an image. With this kind of identification and localization, object detection can be used to count objects in a scene and determine and track their precise locations, all while accurately labeling them.

The focus is to extract the area from the images, so we used python with OpenCV to apply a mask for the image with a threshold to identify the microbubble clearly, then we detected the area of the contours; finally, draw a bounding box with an ID around the microbubbles clusters and choose the largest swarm to track.

4.3.2 Object Tracking

Object tracking has a wide range of applications in computer vision, such as surveillance, human-computer interaction, medical imaging, traffic flow monitoring, and human activity recognition.

Object tracking is the process of taking an input of object detections, then Creating a unique ID for each object of the initial detections, and then tracking each of the objects as they move

around frames in a video, maintaining the assignment of unique IDs.

Furthermore, object tracking allows us to apply a unique ID to each swarm of the microbubbles, making it possible to count them in the video and target the largest one. The algorithm that has been used for microrobots tracking is The centroid tracking algorithm.

The centroid tracking algorithm depends on the centroid extracted by the object tracking. Once we have the bounding box coordinates and the centroid of the microbubbles swarms, we Compute the Euclidean distance between new bounding boxes and the bounding box of the previous frame. If the Euclidean distance is less than a predefined value, we assign the same ID for the object. The performance of the algorithm improves with an increase in the frames per second because we lose the object if there is a time gap between 2 frames. As represented in the Figures 4.6 below, we tracked multiple objects, and we extracted the centroid for each one to use in the feedback system.

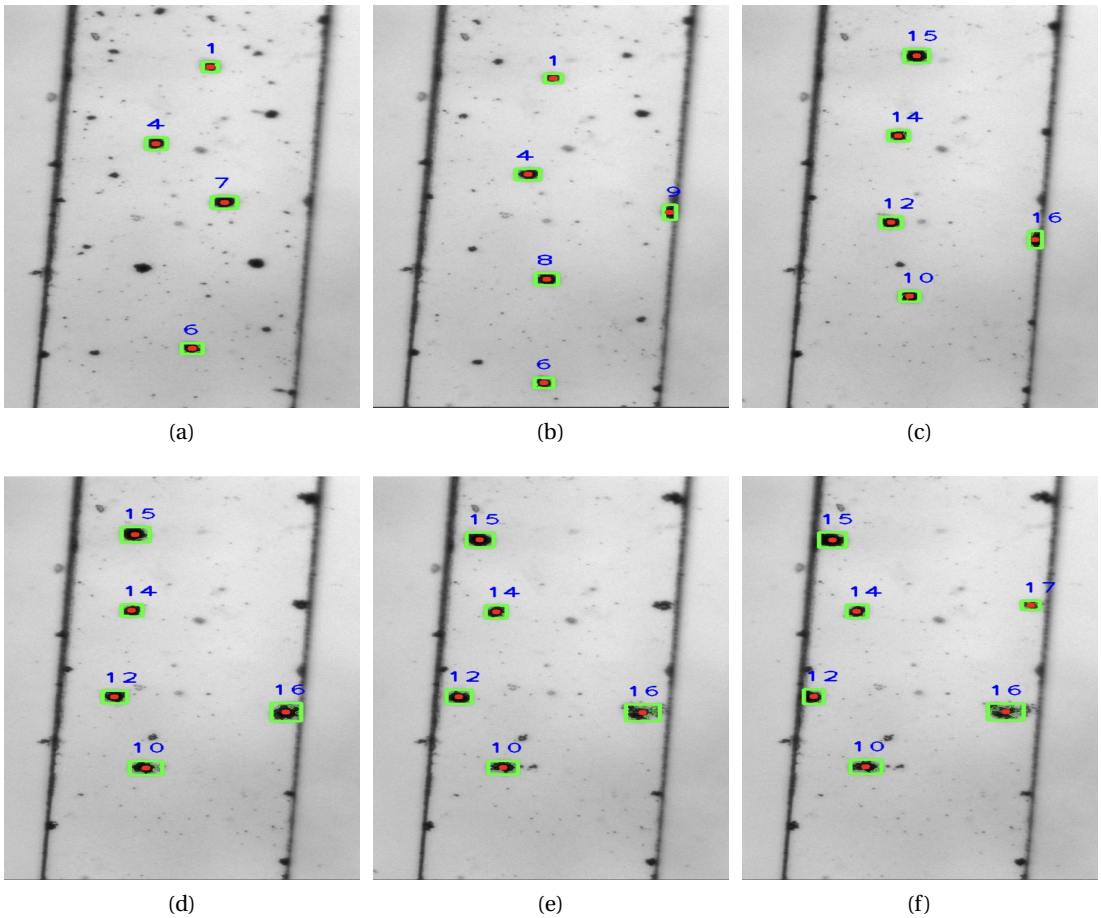

Figure 4.6 – Microrobots with area < 200 pixels

5 Control

5.1 Microrobots

Microrobots are microbubbles based on Resonant Acoustic. The control system of a robot typically consists of a sequence of functional modules that decompose the solution into separate units, such as perception, modeling, planning, and execution.
In fact, this functional division can be traced back to the history and organization of artificial intelligence. For example, perception is typically dealt with using computer vision, which is expected to provide a description of the environment in terms of objects and obstacles. However, computer vision is not necessarily concerned. A large area of artificial intelligence attempts to put together these descriptions into models of environments that can be exploited for planning.

Hardcore robotics consists in designing the physical machine and executing the planned trajectory. Still, besides the mechatronics aspect of the robot design, the control system level question consists of developing suitable automatic methods for finding the sequence of joints, torques, or sound pressure that results in the trajectory demands by the planning system.

This functional decomposition generates controllable, precise, and predictable robotic systems. However, this strategy does not cope well with the uncertainty that is faced by autonomous robots. In addition, since each functional level depends on the previous level to operate, failure at an early stage can paralyze the functioning of the whole control system.

Instead, it's suggested to decompose the problem in terms of competence, as (Brooks, 1986) did. The control system builds the map, looks around, explores, wander, and avoids collision. Each behavior can have direct access to the feedback system, and they could operate in parallel.

5.2 Swarm Robotics

Swarm robotics is the application of the principles of self-organized to the collection of simple, autonomous robots. Simple robots are robots, which do not have sophisticated sensors, electronics, and mechanics and that do not use complex algorithms. The core idea of swarm robotics is to increase simple interactions among robotics in order to solve complex problems, similar to what social insects do.(Floreano and Mattiussi, 2008).

Swarming has also been studied in the context of acoustic work. As mentioned earlier, social insects excel in carrying out physical work that a single animal could not perform. Acoustic swarm microrobots are based on microbubbles mixed with water in a microfluidic channel. When a direct use of acoustic pressure has been used, the time-varying pressure in an acoustic field leads to the oscillation of compressible bodies such as microbubbles. When an oscillating bubble is subjected to a spatial pressure gradient, it experiences an effective net force over its oscillation period called Bjerknes force. If multiple bubbles are nearby, they are not only subjected to the sound pressure field but also by the sound field generated from the neighboring oscillating bubbles, which also generates a force called the second Bjerknes force.

As explained before in Section (2.4), Bjerknes' force could be attractive or repulsive, if the two bubbles are oscillating in phase, then the force is attractive, and if the two bubbles are oscillating out-of-phase, then the force is repulsive (Crum, 1975). In order to observe clearly the swarming phenomena of the microbubbles, we start by filling the microfluidic channel with a solution containing microbubbles and diluted water, and then we apply the acoustic field.

The microbubbles concentration is very high, as represented in Figure (5.1) to recognize how they cluster together to swarm robots. In Figure (5.1)(a) are the microbubbles before applying any acoustic field. After applying the acoustic field, the microbubbles cluster together then the cluster starts to move away from the acoustic field as represented in Figure (5.1)(b) and (c). Regularly, we use less concentration of microbubbles to have fewer swarms to control, but here we used high concentration to show how the bubbles cluster by the effect of the second Bjerknes' force.

Here we refer to the experimental setup of the bifurcation channel with four piezo transducers attached to it, as explained in chapter three. We keep switching between the piezo transducers until all the microbubbles cluster together since if we excite only one piezo transducer, all the microbubbles will cluster and move and attach to the wall. Although we can remove them from the wall by increasing the frequency and the amplitude, it requires more unnecessary tuning for the amplitude and frequency. The bounding box starts to appear around the microbubbles when the area is larger than 300 pixels, as represented in Figure 5.1 (d),(e), and (f).

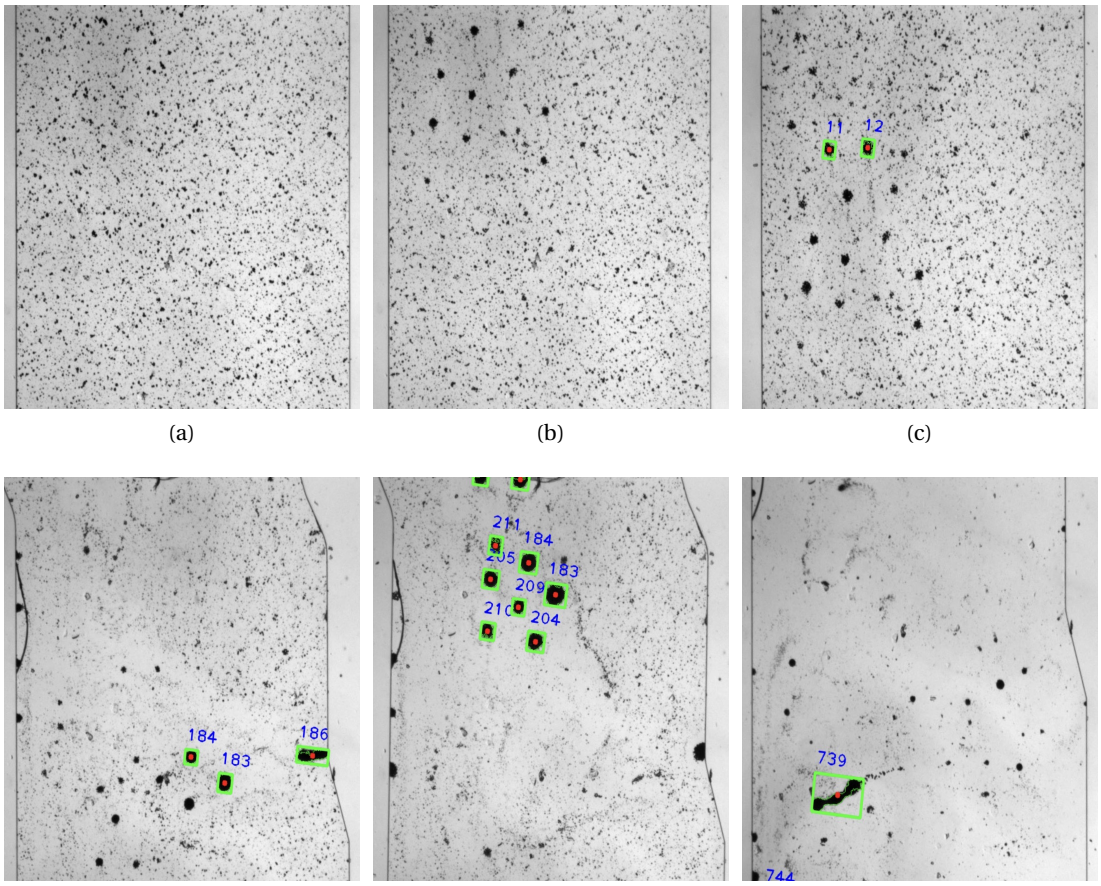

(a) (b) (c)

(d) (e) (f)

Figure 5.1 – Microbubbles cluster to swarms

5.3 Visual Servoing

Visual servoing is a rapidly growing approach to the control of robots that is based on visual perception of robot location. More concretely, visual servoing involves one or more cameras and a computer vision system to control the robot position relative to the target position as required by the task. Modern manufacturing robots can perform the assembly and material handling jobs with speed and precision. Compared to human workers, robots are at a distinct disadvantage since they cannot see what they are doing. Therefore, considerable engineering effort is expended in providing a suitable work environment for these blind machines in industrial applications (Hutchinson et al., 1996).

Based on the camera setup configuration, visual servoing is categorized into eye-in-hand and eye-to-hand visual servoing. It is called an eye-in-hand configuration in situations where the camera is mounted on the robot's end-effector. If the camera is statically installed looking toward the robot and its workspace, the configuration is called eye-to-hand. We refer to the configurations where the camera is fixed and look to the microrobots and the environment.

5.3.1 Visual servoing strategy

Based on the ways in which the visual feedback is used to control the robot, visual servoing is classified into two different classes, Image-Based Visual Servoing (IBVS), Position-Based Visual Servoing (PBVS) (Hutchinson et al., 1996). Each of these strategies is discussed separately in the following sections.

Position Based Visual Servoing

In a position-based visual servoing (PBVS) controller, the position and orientation of the object are extracted from the image captured by the camera. Comparing the object position and orientation with the desired ones, the position and orientation errors are computed as the input to the controller. The PBVS controller generates a controlling signal to reduce the relative position and orientation errors. Finally, a joint level servo controller tracks the controlling command produced by the Cartesian controller. The block diagram of a PBVS controller is shown in Figure5.2.

The robot control problem is prevalent and well established. Thus, the main challenge is the robustness, accuracy, and speed of computing the object position and orientation. Besides, in order to be able to calculate the object pose, a complete geometric model of the object is needed. Furthermore, using PBVS, no control is available on the image trajectory and the object may leave the camera's field of view (FOV), which causes the visual servoing task to fail.

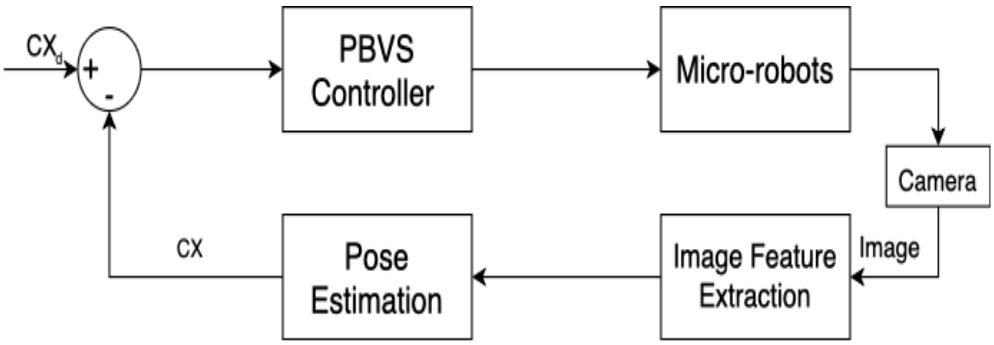

Figure 5.2 – Position based visual servoing block diagram

Image Based Visual Servoing

In image-based visual servoing (IBVS), the control commands are computed based on the image features data directly. The difference between the current features and the desired ones creates the visual servoing error, and the controller moves the robot to reduce this error until it becomes zero. Figure 5.3 , shows the structure of an IBVS controller. Image features usually used in this approach could be the position of points, size of a region, center of a region, length of a line, segment, and rotation angle of a line.

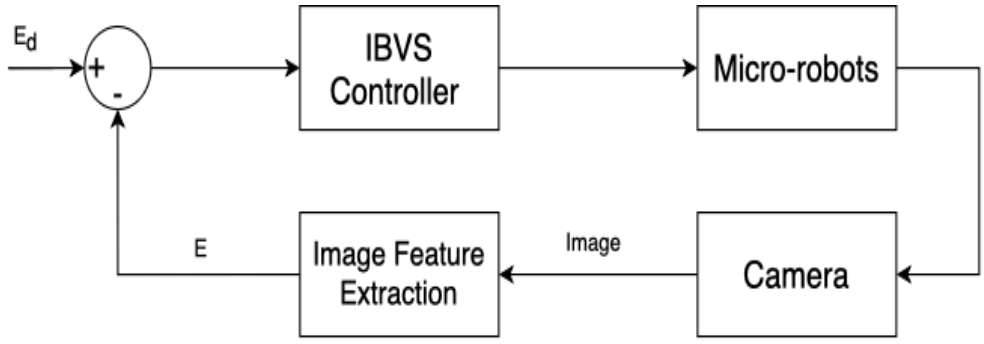

Figure 5.3 – Image based visual servoing block diagram

Considering the two controllers mentioned above, PBVS will be more effective if we want to move the base of the microscope with the microchannels on it, so we can have a target position not only on the field of view of the camera but also at any point in the channel. We refer here to the IBVS since we focused more on manipulating the microrobots where the camera field of view was covering the whole channel. Moreover, to track the microrobots in a chaotic flow, we needed to fix the camera and the environment because of moving any of them will easily lead to loose tracking of the microrobots.

5.3.2 Visual Servoing Controller

The control system for the microrobot swarms moving inside the microfluidic channels depends on how many piezotransducer is excited at a time. Moreover, it depends on how many actuators are used in the system. We referred to two cases using four or six piezo transducers, which are not the limits; we can still use more actuators to move more accurately in our environment.

The control system for a single swarm without considering the attraction forces between any other swarms in the system is close to the unicycle model. Turning on a transducer, the swarm move away from it perpendicularly so the angel can be controlled by the position of each piezo transducer. The piezo transducers are placed at the middle of the microfluidic channel; when we consider the area where the microrobots are close to the center of the piezo, the microrobots move perfectly perpendicular to the transducer, but if we are at any of the transducer sides, the microrobots move perpendicular with extra ten degrees to this side (Dual and Möller, 2012). A simplified kinematic model for the microbubbles swarm without considering the interaction between neighboring objects can be expressed as

$$\dot{x} = v cos(\theta) \qquad \dot{y} = v sin(\theta) \qquad \dot{\theta} = \omega \tag{5.1}$$

Where (v) is velocity calculated by dividing the Euclidian distance between the current and previous frames, and the time, which is one divided by numbers of frames per second, (θ)

for simplification and as observed from the experiments are considered perpendicular to the piezo transducer since we are using four transducer (θ) is equal ($n\pi/2$) where n is the piezo number. ($\dot{y}$), ($\dot{x}$), and (ω) are the horizontal, vertical, and angular velocities, respectively. Suppose we have more than four transducers as represented in experimental setup two in Subsection(3.2.2), six transducers adhered to the microfluidic channel, four of them with ($\pi/4$), which increases the possible values of (θ). Although exiting more than one piezo transducer at the same time will allow more controllability for the angel, the dynamic of the system and combination of the acoustic field leads to unexpected results as perceived from the experiments, which leads us to excite a single piezo actuator at a time.

As mentioned in equation (5.1), we consider the kinematic model for the micro-robots as the unicycle model. In the Figure (5.4), we state the inputs to the model as the velocity (v) and the orientation (θ).

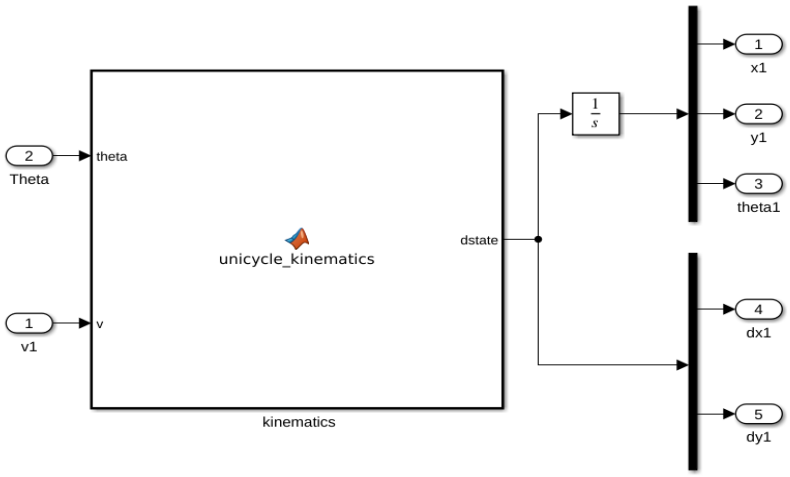

Figure 5.4 – Representation for the Kinematic model using Matlab

The outputs from the model are the (x) and (y), which are used to calculate the Euclidian distance (ϵ) to minimize it by minimizing the error in the two directions where (e_x) and (e_y) are the errors in x and y directions, respectively

$$e_x = x_d - x \qquad\qquad e_y = y_d - y \tag{5.2}$$

Where (x_d) and (y_d) are the goal position. Achieving the perfect orientation was not crucial in the application since the target is to reach the goal point and then releases the drugs, which does not require a specific orientation, and (dx) and (dy) are extracted to observe the velocity in the two directions.

Conditional sentences are constructed to minimize the error by choosing which electric piezo transducer to excite. The break condition was the euclidean distance (ϵ), which is an accepted error from the goal position.

Two techniques have been followed while writing the code for the visual servoing. The first approach is to target the largest swarm and choose a specific target to reach in the (x) and (y) directions, then measure the error in $(x)$and (y)between the center of the swarm and the target, then excite the corresponding piezo to move the swarm to the target. The second approach is to split the image into nine boxes and then apply a sequence from the position of the largest swarm to one of the boxes since the target of manipulating the microrobots is to reach a specific area, so it was still a feasible approach to target a specific area rather than a point because we don't need to calculate the error at each frame, but we extract at which box the swarm exists, and according to that we excite the corresponding transducer.

5.4 Operating Modes

As described in chapter four, python and Matlab have been used to interface with the function generator, control circuit, and camera. Although with Matlab, it was not possible to achieve a visual feedback control system during the low speed of image acquisition, it was very efficient to interface with the joystick to switch between the piezo transducer and learn the ranges of the frequencies and amplitudes that drive the microrobots efficiently. Python has been used for the visual feedback system since the acquisition was fast to detect and track the microrobots, and the manual mode interface has been implemented by the keyboard to test the piezo transducers.

There are four operating modes available to test and drive the microrobots. Each of these modes is discussed separately in the next section.

5.4.1 Manual

The system consists of the Logitech joystick, control circuit with an Arduino Uno microcontroller, and Hamamatsu camera, all of them connected to the Matlab. The joystick has two axes that represent the four directions, and every direction is assigned to one piezo transducer. The function generator produces an AC sine wave, and it's connected to the high voltage part of the relay circuit, as explained before in Subsection (3.5.2). Moreover, the function generator is controlled with a custom-made driver with Matlab through the joystick. Ten extra buttons of the joystick are used to change the modes and the driving frequencies and amplitudes. Button one is used to go to the transducer's resonant frequency, which is $240kHz$ and $2Volt$ as amplitude, then the second button is used to go to testing mode. Four buttons are used for changing the frequency with different ranges, two buttons for $(+or-1000Hz$)and two buttons for $(+or-10Hz)$. The last four buttons are used to adjust the amplitude, two buttons for $+or-0.1V$ and two buttons for $+or-0.01V$. As a result of controlling the whole system from the joystick by watching how the system behaves from the live streaming coming from the camera, it was possible to find the best values to use for manipulation as well as the best values to start with at the case of visual feedback mode. Besides, manual mode is a reasonable way in medical application because of the unexpected complexities that we might face.

5.4.2 Testing

Testing mode is recommended before using the manual or the vision feedback control since the connections of the piezo transducers are fragile and easily get unattached from the piezo transducer surface. Button two from the joystick is used to set the frequency to $10kHz$ and the amplitude to $5V$, which are in the human hearing range, so you can hear a beep sound from the exited piezo-transducers. The range of the human range is from $2to20kHz$ and the amplitude range available from the function generator is from $0to20V$ since the piezo transducers are glued to the surface of the microfluidic channel, the amount of the glue used defines the damping force on the piezo transducer. Furthermore, if the damping force is high, it is possible to change the frequency and amplitude by using the same buttons as explained before in the manual mode to hear the beep of the transducer, which indicates that it's connected.

5.4.3 Tuning

Tuning mode depends mainly on the vison feedback control, which is implemented using the python programming language. As mentioned before, the target frequency is the resonant frequency. Still, every piezo transducer has a slightly different resonant frequency, and when the microrobots cluster to big swarms, they stop responding to the same frequency, and they require higher amplitude to keep moving. In addition, when the micro-robot swarms move farther away from the piezo transducer, the acoustic radiation force decreases, and in order to keep them moving at a constant speed, a higher amplitude is needed to increase the radiation force. As mentioned before in Section (2.4), the micro-robot swarms tend to move towards the wall where the drag force is more diminutive, and they attach to the wall due to the surface tension and second radiation force, which show that with a lower value of the amplitude, the micro-robots can preserve the same velocity.

After using the manual mode to study the system, we observed that the resonant frequency ranges from 235 to $250kHz$ and the micro-robots start to move with a value of $2V$ for the amplitude, so we fix the amplitude and turn on one of the transducers then change the frequency until we detect the movement of the swarms, then we save each transducer resonant frequency in a different variable. After fixing the frequency, we detect the largest swarm as the main target to drive and track. As mentioned before in Section (4.3), the Euclidean distance is measured by the object tracing, and by knowing that the camera captures (50) frames per second, we obtain the velocity, as the Euclidean distance divided by the time, which depends on how many frames per second acquired. The measured velocity unit is in pixels per second, and it's tuned by a state machine controller to keep the speed constant.

5.4.4 Vision Feedback Control

In the beginning, we started using Matlab with the objective of reaching a target point in the microfluidic channel with planning a path from the initial point to the final point. Later we found that to plan the path, we have to consider the dynamic behavior of the system because of the second radiation forces which attract the swarms to each other, so we used the Image-Based Visual Servoing (IBVS) approach to move the micro-robots and track them all the time to reach the target as we mentioned before in Subsection (5.3.2), we used two techniques either to choose a certain point at the image or, we choose one of the nine boxes.

We observed from the experiments that moving the micro-robots swarms are either close to the wall because they don't face the drag forces and the effect of the other clusters is less because they are sticking to the wall with the surface tension. Moreover, it is very clear that the system is a complicated system due to the dynamic behavior that has been observed during the experiments since under some cases, the micro-robots doesn't respond to the used ranges of frequencies, and in some other cases, when they are so close to the piezo transducer the effect of the high amplitude make the microbubbles to lose their properties and stick to the channel, then we need to flush the microfluidic channel and repeat the experiments. As mentioned before, a python custom code has been used to interface with the whole system, but at any point, you can stop the system by pressing the escape button and go to the manual control from the keyboard arrows with the preset values saved for each piezo transducer.

5.5 Experimental Results

Experiments have been done for all the cases to understand the system as in manual mode, testing mode, and tuning mode. In this section, we will focus on some of the experiment results coming from the image feedback system. As represented in Table (5.1), five test cases have been stated. The first case measures the accuracy and the velocity, and the next three cases are a comparison in the same environment, but with changing the micro-robots. Finally, the last case states some limitations have been observed in the system.

Table 5.1 – Experimental results for five test cases

Test case	Channel	Accuracy	Accepted
1	4 piezo-square channel	Euclidean distance< 20	yes
2	4 piezo-Bifurcation channel	Euclidean distance< 20	yes
3	4 piezo-Bifurcation channel	Euclidean distance< 50	yes
4	4 piezo-Bifurcation channel	Euclidean distance< 50	yes
5	4 piezo-Bifurcation channel	Euclidean distance> 50	No

5.5.1 Test Case 1

The first experiment is a simple test case to analyze the system. We observed from the experiments that the Micro-robot swarm reached the target, but trying to tune the speed with a PI controller didn't lead to good results since the actuators required time to switch off and on from 5 to 15 ms. When the velocity measure is zero, the PI increases the amplitude with a high value, leading to losing the swarm's control. A simple tunning method has been used with a simple loop condition. When the swarms stop moving or the speed decreases, we increase the amplitude with ($0.1 Volt$), which is observed from the experiments that it's a better way to control the speed.

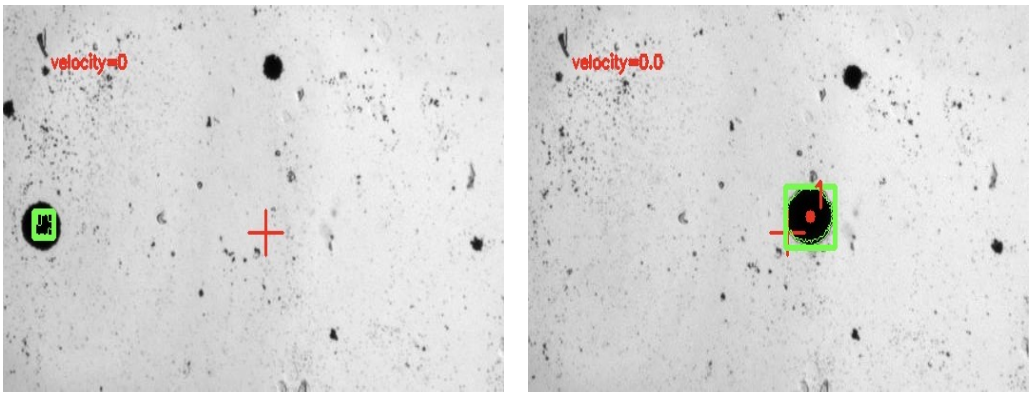

(a) Start position (b) Goal Position

Figure 5.5 – Test case 1

In the Figure represented below (5.6(a)), it's a path from the initial to the final position, the robot reaches the target in less than five seconds since it's a short distance and a simple environment, then in the next Figure (5.6 (b)), we recorded the inputs to the actuators in this case Piezo left was not turning on during the experiment so in the graph, the other three piezo transducers are represented. The (x) axis represents the frame number, and the camera records 20 frames/second, so we can also observe the time.

The last Figure represents the speed, which is measured by the use of the euclidian distance and the frame rate per second. The reference speed is $50 Pixels/s$. We can observe clearly that the speed values deviate all the time, but this deviation is due to the object detection because when the feedback detects a different swarm moving faster since it's smaller leads to this deviation in the measurements. The solution was to use a threshold in the loop condition and consider the reasonable readings for the velocity, then adjust the amplitude according to these readings.

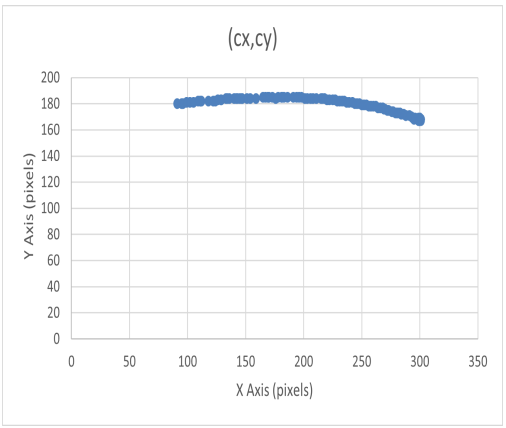

(a) Robot Path

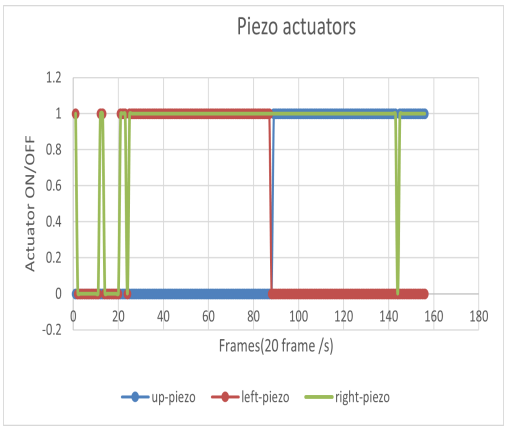

(b) Piezo actuator signal

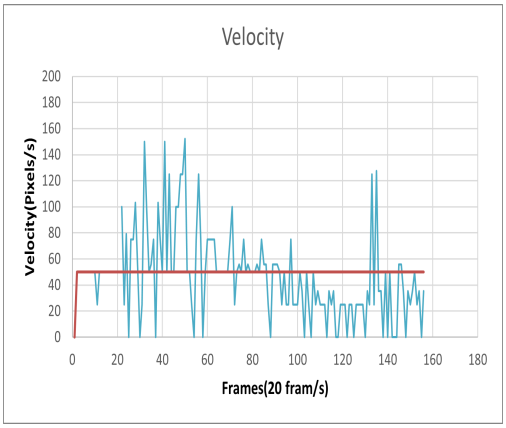

(c) velocity diagram

Figure 5.6 – Test case 1 charts

5.5.2 Test Case 2

The second experiment is consists of three trials to drive the micro-robots to the same location in the same channel(bifurcation channel). It's a complicated task to repeat the same experiment since we need to flush the micro-robot swarms outside the channel, inject new microbubbles, cluster them, and manually try to lead the swarm to the same position. Finally, run the image feedback controller. The micro-robots stop when the error becomes close to zero with a specific threshold, which depends on the image resolution. In this case, the threshold is 50 pixels.

In the Figure below (5.7), we represent the initial and final position of one of the three experiments in the bifurcation channel since they are very close to each other.

Figure (5.7) shows the three micro-robot positions plotted on the same graph. Although the path is different, we observed that the microrobots always try to reach the final task. In our case, path planning was not crucial since there were no obstacles inside the channels.

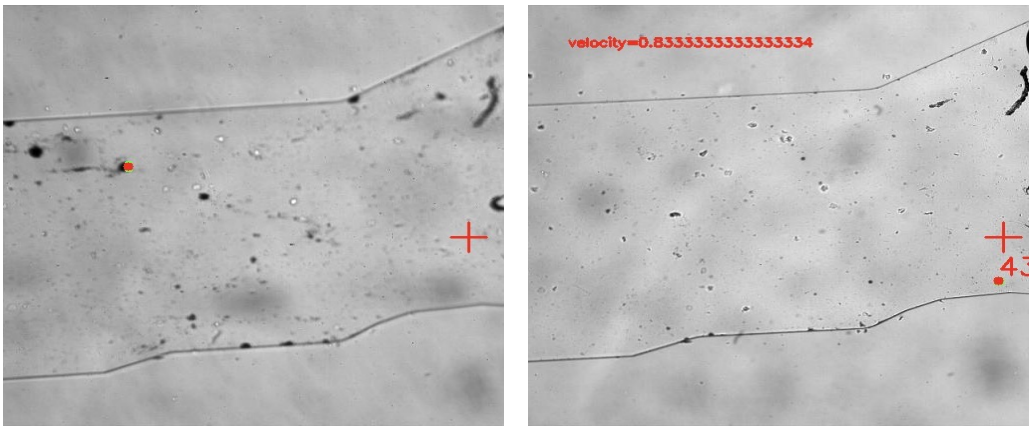

(a) Start position (b) Goal Position

Figure 5.7 – Test case 2

Figure (5.8) shows the three micro-robot positions plotted on the same graph. Although the path is different, we observed that the microrobots always try to reach the final task. In our case, path planning was not crucial since there were no obstacles inside the channels.

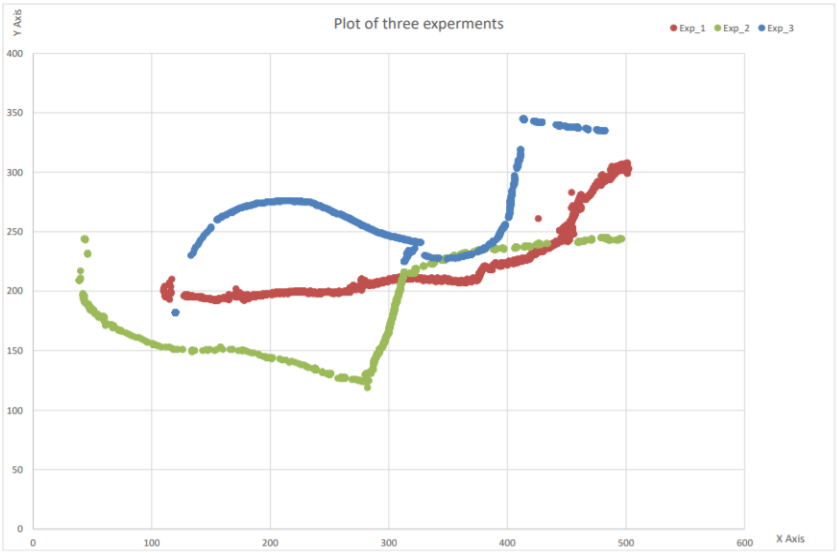

Figure 5.8 – Position of micro-swarm for three experments

5.5.3 Test Case 3

This test case has been conducted in the bifurcation channel, which shows that when we are far away from the piezo transducer, even with the maximum voltage ($20Vpp$), we cannot reach the target location. In this case, the right piezo actuator was required to make the micro-robot swarm number (19) in the Figure (5.9(b)) reach the target, but there was not enough voltage to move the swarm. The solution is to use an amplifier to amplify the voltage so the sound waves can penetrate more to the end of the channel.

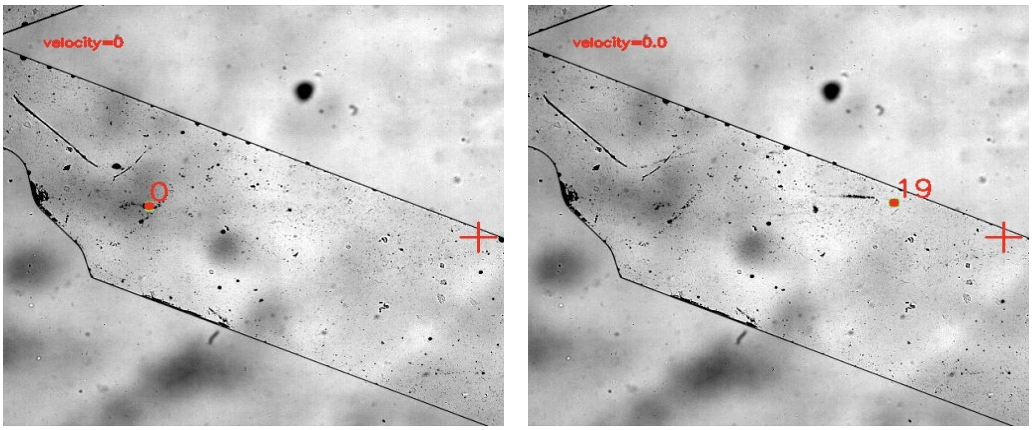

(a) Start position (b) Goal Position

Figure 5.9 – Test case 3

6 Conclusions

A targeted drug delivery technology using acoustic excitation of microbubble swarms is introduced and experimentally validated. In the first part (Chapter. 2), we preliminarily focused on the study of the physics of the microbubbles in the microfluidic channels, and then the mathematical model of the acoustic radiation force generated by the acoustic field was introduced after the simplification that has been done by using the perturbation theory. Moreover, the effect of the second Bjerknes force and drag force has been explained, which developed the dynamic behavior for the system.

Then the system components have been illustrated in (Chapter .3), differentiating between using Matlab and python programming language to interface with the whole control system. In addition, several experimental setups have been designed to test the micro-swarms behavior in a different environment and with different numbers of transducers. Later a better method for coupling was explained to facilitate using the piezoelectric transducers without adhering them to the surface of any kind of environment. Afterward, we explained different approaches and algorithms for image processing to detect and track the micro-robot swarms, and the resulting tracker was able to efficiently track the swarms, then assign a unique ID for every swarm and calculate the Euclidian distance between the current and previous frame for the same swarm.

The velocity of the swarms has been measured by using the Euclidian distance and the frame rate per second. In (Chapter 5) these results are used in most of the operating modes. The manual mode through the joystick obtained full control for testing, tunning, and driving the micro-robots to any location in the microfluidic channel. After explaining the swarming behavior of the micro-bubbles, visual servoing feedback control has been described with PI controller to tune the driving amplitude of the piezo actuator to keep the targeted micro-robots speed constant all over the channel.

Real experiments showed that the microbubbles cluster together and become larger, which requires a higher amplitude to move them. On the other hand, if the amplitude is very high and a piezo transducer is turned on while a micro-robot swarm is near it, this micro-robot

loses its properties and sticks to the wall. Moreover, moving the microrobots close to the wall leads to higher performance since the drag force decreases, and with less amplitude, you can keep driving the micro-robots. Finally, the target of the microrobots is to facilitate the drug delivery to specific areas in the human body, so targeting an area of the image as a destination was more efficient than targeting a specific point to reach.

6.1 Future Work

In this work, important aspects have been found regarding the implementation of Image-Based visual servoing controller that the microscope image does not cover the whole channel, so a coordinate system for the channel itself will make it possible to reach any position in the channel, not just the field of view of the camera. Moreover, considering the dynamic behavior of the system, precisely the second Bjerknes force, by considering the size of each cluster. Measuring the effect of this force in real-time delayed the visual feedback control system, so by using a workstation computer, it would be possible to consider the influence of the dynamic behavior in the system.

Considering more complicated 3D channel designs and proving the possibility to go for mice trials, since the microbubbles have already clinical approval and as mentioned in section (3.3), the echo flex design of the piezoelectric transducer housing is meant to be placed on a mouse head with collaborating with the university hospital of Zurich. Other research directions include training the micro-robots directly in a closed loop with a reinforcement learning approach, using more complex features such as trajectory predictions, and learning from real demonstrations of manual manipulation tasks.

Bibliography

Ahmed, D., Baasch, T., Blondel, N., Läubli, N., Dual, J., & Nelson, B. J. (2017). Neutrophil-inspired propulsion in a combined acoustic and magnetic field. *Nature communications*, *8*(1), 1–8.

Ahmed, D., Baasch, T., Jang, B., Pane, S., Dual, J., & Nelson, B. J. (2016). Artificial swimmers propelled by acoustically activated flagella. *Nano letters*, *16*(8), 4968–4974.

Ahmed, D., Ozcelik, A., Bojanala, N., Nama, N., Upadhyay, A., Chen, Y., Hanna-Rose, W., & Huang, T. J. (2016). Rotational manipulation of single cells and organisms using acoustic waves. *Nature communications*, *7*(1), 1–11.

Ashkin, A., & Dziedzic, J. M. (1987). Optical trapping and manipulation of viruses and bacteria. *Science*, *235*(4795), 1517–1520.

Baker, N. V. (1972). Segregation and sedimentation of red blood cells in ultrasonic standing waves. *Nature*, *239*(5372), 398–399.

Beebe, D. J., Mensing, G. A., & Walker, G. M. (2002). Physics and applications of microfluidics in biology. *Annual review of biomedical engineering*, *4*(1), 261–286.

Bjerknes, V. (1906). *Fields of force: supplementary lectures, applications to meteorology; a course of lectures in mathematical physics delivered december 1 to 23, 1905*. Columbia University Press.

Brooks, R. (1986). A robust layered control system for a mobile robot. *IEEE journal on robotics and automation*, *2*(1), 14–23.

Bruus, H. (2008). *Theoretical microfluidics* (Vol. 18). Oxford university press Oxford.

Bruus, H. (2012). Acoustofluidics 2: perturbation theory and ultrasound resonance modes. *Lab on a Chip*, *12*(1), 20–28.

Coakley, W. T., Bardsley, D. W., Grundy, M. A., Zamani, F., & Clarke, D. J. (1989). Cell manipulation in ultrasonic standing wave fields. *Journal of Chemical Technology & Biotechnology*, *44*(1), 43–62.

Crum, L. A. (1975). Bjerknes forces on bubbles in a stationary sound field. *The Journal of the Acoustical Society of America*, *57*(6), 1363–1370.

De Vlaminck, I., & Dekker, C. (2012). Recent advances in magnetic tweezers. *Annual review of biophysics*, *41*, 453–472.

Dey, S. (2018). *Hands-on image processing in python*.

Dolzhansky, F. V. (2013). Equations of motion of an ideal incompressible fluid; kelvin's circulation theorem. *Fundamentals of geophysical hydrodynamics* (pp. 3–11). Springer.

Dual, J., & Möller, D. (2012). Acoustofluidics 4: piezoelectricity and application in the excitation of acoustic fields for ultrasonic particle manipulation. *Lab on a Chip*, *12*(3), 506–514.

Dual, J., & Schwarz, T. (2012). Acoustofluidics 3: continuum mechanics for ultrasonic particle manipulation. *Lab on a Chip*, *12*(2), 244–252.

Dual, J., & Möller, D. (2014). Piezoelectricity and application to the excitation of acoustic fields for ultrasonic particle manipulation. *Microscale acoustofluidics* (pp. 81–99). Royal Society of Chemistry Cambridge.

Esteban-Fernández de Ávila, B., Angell, C., Soto, F., Lopez-Ramirez, M. A., Báez, D. F., Xie, S., Wang, J., & Chen, Y. (2016). Acoustically propelled nanomotors for intracellular sirna delivery. *Acs Nano*, *10*(5), 4997–5005.

Floreano, D., & Mattiussi, C. (2008). *Bio-inspired artificial intelligence: theories, methods, and technologies*. MIT press.

Gao, W., Zhang, X., Yang, L., & Liu, H. (2010). An improved sobel edge detection. *2010 3rd International conference on computer science and information technology*, *5*, 67–71.

Garcia-Sabaté, A., Castro, A., Hoyos, M., & González-Cinca, R. (2014). Experimental study on inter-particle acoustic forces. *The Journal of the Acoustical Society of America*, *135*(3), 1056–1063.

Gor'kov, L. P. (1962). On the Forces Acting on a Small Particle in an Acoustical Field in an Ideal Fluid. *Soviet Physics Doklady*, *6*, 773.

Guo, B., & Hong, M.-C. (1993). The landau-lifshitz equation of the ferromagnetic spin chain and harmonic maps. *Calculus of Variations and Partial Differential Equations*, *1*(3), 311–334.

Hartigan, J. A., & Wong, M. A. (1979). Algorithm as 136: a k-means clustering algorithm. *Journal of the royal statistical society. series c (applied statistics)*, *28*(1), 100–108.

Hertz, H. (1995). Standing-wave acoustic trap for nonintrusive positioning of microparticles. *Journal of applied physics*, *78*(8), 4845–4849.

Hutchinson, S., Hager, G. D., & Corke, P. I. (1996). A tutorial on visual servo control. *IEEE transactions on robotics and automation*, *12*(5), 651–670.

Juan, M. L., Righini, M., & Quidant, R. (2011). Plasmon nano-optical tweezers. *Nature photonics*, *5*(6), 349–356.

Laurell, T., & Lenshof, A. (2014). *Microscale acoustofluidics*. Royal Society of Chemistry.

Li, T., Chang, X., Wu, Z., Li, J., Shao, G., Deng, X., Qiu, J., Guo, B., Zhang, G., He, Q., et al. (2017). Autonomous collision-free navigation of microvehicles in complex and dynamically changing environments. *Acs Nano*, *11*(9), 9268–9275.

Marzo, A., & Drinkwater, B. W. (2019). Holographic acoustic tweezers. *Proceedings of the National Academy of Sciences*, *116*(1), 84–89.

Mohanty, S., Khalil, I. S., & Misra, S. (2020). Contactless acoustic micro/nano manipulation: a paradigm for next generation applications in life sciences. *Proceedings of the Royal Society A*, *476*(2243), 20200621.

Nagargoje, M., & Gupta, R. (2020). Effect of sinus size and position on hemodynamics during pulsatile flow in a carotid artery bifurcation. *Computer methods and programs in biomedicine*, *192*, 105440.

Nelson, B. J., Kaliakatsos, I. K., & Abbott, J. J. (2010). Microrobots for minimally invasive medicine. *Annual review of biomedical engineering, 12*, 55–85.

Neuman, K. C., & Nagy, A. (2008). Single-molecule force spectroscopy: optical tweezers, magnetic tweezers and atomic force microscopy. *Nature methods, 5*(6), 491–505.

Ozcelik, A., Rufo, J., Guo, F., Gu, Y., Li, P., Lata, J., & Huang, T. J. (2018). Acoustic tweezers for the life sciences. *Nature methods, 15*(12), 1021–1028.

Shi, J., Ahmed, D., Mao, X., Lin, S.-C. S., Lawit, A., & Huang, T. J. (2009). Acoustic tweezers: patterning cells and microparticles using standing surface acoustic waves (ssaw). *Lab on a Chip, 9*(20), 2890–2895.

Soltani, M. K., Khanmohammadi, S., Ghalichi, F., & Janabi-Sharifi, F. (2017). A soft robotics nonlinear hybrid position/force control for tendon driven catheters. *International Journal of Control, Automation and Systems, 15*(1), 54–63.

Tang, S., Zhang, F., Zhao, J., Talaat, W., Soto, F., Karshalev, E., Chen, C., Hu, Z., Lu, X., Li, J., et al. (2019). Structure-dependent optical modulation of propulsion and collective behavior of acoustic/light-driven hybrid microbowls. *Advanced Functional Materials, 29*(23), 1809003.

Tian, Z., Yang, S., Huang, P.-H., Wang, Z., Zhang, P., Gu, Y., Bachman, H., Chen, C., Wu, M., Xie, Y., et al. (2019). Wave number–spiral acoustic tweezers for dynamic and reconfigurable manipulation of particles and cells. *Science advances, 5*(5), eaau6062.

Urschel, K., Tauchi, M., Achenbach, S., & Dietel, B. (2021). Investigation of wall shear stress in cardiovascular research and in clinical practice—from bench to bedside. *International Journal of Molecular Sciences, 22*(11), 5635.

Wu, Z., Troll, J., Jeong, H.-H., Wei, Q., Stang, M., Ziemssen, F., Wang, Z., Dong, M., Schnichels, S., Qiu, T., et al. (2018). A swarm of slippery micropropellers penetrates the vitreous body of the eye. *Science advances, 4*(11), eaat4388.

Xu, T., Soto, F., Gao, W., Dong, R., Garcia-Gradilla, V., Magaña, E., Zhang, X., & Wang, J. (2015). Reversible swarming and separation of self-propelled chemically powered nanomotors under acoustic fields. *Journal of the American Chemical Society, 137*(6), 2163–2166.

Yosioka, K., & Kawasima, Y. (1955). Acoustic radiation pressure on a compressible sphere. *Acta Acustica united with Acustica, 5*(3), 167–173.

Zhang, S. P., Lata, J., Chen, C., Mai, J., Guo, F., Tian, Z., Ren, L., Mao, Z., Huang, P.-H., Li, P., et al. (2018). Digital acoustofluidics enables contactless and programmable liquid handling. *Nature communications, 9*(1), 1–11.